

# First results from the IllustrisTNG simulations: radio haloes and magnetic fields

Federico Marinacci<sup>1\*</sup>, Mark Vogelsberger<sup>1</sup>, Rüdiger Pakmor<sup>2</sup>, Paul Torrey<sup>1</sup>,  
Volker Springel<sup>2,3</sup>, Lars Hernquist<sup>4</sup>, Dylan Nelson<sup>5</sup>, Rainer Weinberger<sup>2</sup>,  
Annalisa Pillepich<sup>6</sup>, Jill Naiman<sup>4</sup>, Shy Genel<sup>7,8</sup>

<sup>1</sup>Kavli Institute for Astrophysics and Space Research, Massachusetts Institute of Technology, Cambridge, MA 02139, USA

<sup>2</sup>Heidelberger Institut für Theoretische Studien, Schloss-Wolfsbrunnengasse 35, D-69118 Heidelberg, Germany

<sup>3</sup>Zentrum für Astronomie der Universität Heidelberg, Astronomisches Recheninstitut, Mönchhofstr. 12-14, D-69120 Heidelberg, Germany

<sup>4</sup>Harvard-Smithsonian Center for Astrophysics, 60 Garden Street, Cambridge, MA 02138, USA

<sup>5</sup>Max-Planck-Institut für Astrophysik, Karl-Schwarzschild-Straße 1, D-85741 Garching bei München, Germany

<sup>6</sup>Max-Planck-Institut für Astronomie, Königstuhl 17, D-69117, Heidelberg, Germany

<sup>7</sup>Center for Computational Astrophysics, Flatiron Institute, 162 Fifth Avenue, New York, NY 10010, USA

<sup>8</sup>Columbia Astrophysics Laboratory, Columbia University, 550 West 120th Street, New York, NY 10027, USA

Accepted 2018 August 10. Received 2018 August 08; in original form 2017 July 12.

## ABSTRACT

We introduce the IllustrisTNG project, a new suite of cosmological magnetohydrodynamical simulations performed with the moving-mesh code AREPO employing an updated Illustris galaxy formation model. Here we focus on the general properties of magnetic fields and the diffuse radio emission in galaxy clusters. Magnetic fields are prevalent in galaxies, and their build-up is closely linked to structure formation. We find that structure formation amplifies the initial seed fields ( $10^{-14}$  comoving Gauss) to the values observed in low-redshift galaxies ( $1 - 10 \mu\text{G}$ ). The magnetic field topology is closely connected to galaxy morphology such that irregular fields are hosted by early-type galaxies, while large-scale, ordered fields are present in disc galaxies. Using two simple models for the energy distribution of relativistic electrons we predict the diffuse radio emission of 280 clusters with a baryonic mass resolution of  $1.1 \times 10^7 M_\odot$ , and generate mock observations for VLA, LOFAR, ASKAP and SKA. Our simulated clusters show extended radio emission, whose detectability correlates with their virial mass. We reproduce the observed scaling relations between total radio power and X-ray emission,  $M_{500}$ , and the Sunyaev-Zel'dovich  $Y_{500}$  parameter. The radio emission surface brightness profiles of our most massive clusters are in reasonable agreement with VLA measurements of Coma and Perseus. Finally, we discuss the fraction of detected extended radio haloes as a function of virial mass and source count functions for different instruments. Overall our results agree encouragingly well with observations, but a refined analysis requires a more sophisticated treatment of relativistic particles in large-scale galaxy formation simulations.

**Key words:** magnetic fields – MHD – methods: numerical – cosmology: theory – radio continuum: general – galaxies: clusters: general

## 1 INTRODUCTION

The ubiquitous presence of magnetic fields in the Universe is an established observational fact (Beck & Wielebinski 2013). The progress of observational techniques has allowed for the measurement of the present-day field intensities and the mapping of their orientations with an increasing degree of accuracy. The situation is far more uncertain in low-density environments, such as cosmological filaments and voids, where a robust detection is still lacking.

Indeed, the considerably lower field strength expected in those regions ( $\lesssim 1 \text{ nG}$ ) makes a direct detection very challenging. This lack of detections on large scales is particularly unfortunate because it leaves us with very little information about the origin of magnetic fields and their subsequent amplification during structure formation.

Magnetic fields are also an essential component of many astrophysical phenomena occurring at all scales. It is now generally known that clusters are permeated by magnetic fields that extend into the intergalactic medium. The existence of those large-scale ( $\sim 1 \text{ Mpc}$ ) fields is inferred through Faraday rotation sig-

\* E-mail: fmarinac@mit.edu

nals of polarized radio galaxies (Murgia et al. 2004; Govoni et al. 2006; Guidetti et al. 2008; Bonafede et al. 2010) and extended synchrotron radio emission (e.g. Feretti et al. 2012), which cannot be directly associated to individual galaxies hosting an active galactic nucleus (AGN). This radio emission can be broadly divided in three categories: (i) radio relics, which are predominantly found in the outskirts of clusters and trace mergers and shocks, (ii) (giant) radio haloes, that show a more regular morphology and whose emission is predominantly unpolarized, appears to be approximately centred on the X-ray emission of the cluster and extends on scales of  $\sim 1$  Mpc, and (iii) mini radio haloes associated to relaxed clusters and extending on smaller ( $\sim 50 - 300$  kpc) scales. Diffuse radio emission from clusters has been extensively studied since it is an important tool to unveil the complex interplay among physical processes occurring in the intracluster medium (ICM). Indeed, these diffuse radio sources are very sensitive to the microphysics of the ICM, such as turbulence level and shock structures, and thus they represent an important probe to determine its properties.

Despite extensive observational campaigns, many aspects of the diffuse radio emission in clusters are still poorly understood. For example, there is no definitive model to explain their origin. Given the short cooling time of electrons emitting synchrotron radiation, an efficient mechanism that re-accelerates them or injects fresh electrons at relativistic speeds is needed to maintain radio emission on Mpc scales. Two main models have been proposed. In one scenario, relativistic electrons are produced by hadronic interactions of cosmic ray protons with the ICM (e.g. Blasi & Colafrancesco 1999; Pfrommer et al. 2008; Enßlin et al. 2011). A mechanism to accelerate protons at relativistic speed is thus needed, and several of them, like accretion shocks or feedback from AGN and galactic winds, might be at work. In the second scenario, local re-acceleration of electrons occurs through interaction with plasma waves driven by turbulence in the ICM, possibly caused by cluster mergers/assembly (Giovannini et al. 1993; Brunetti et al. 2009; Donnert et al. 2013). Each of these models has its difficulties. For instance, the classic hadronic scenario predicts in galaxy clusters a level of gamma-ray emission from inelastic collision between the cosmic ray protons and thermal protons in the ICM that is in tension with the persistent non-detections coming from the *Fermi* satellite (Ackermann et al. 2016). While this can be somewhat mitigated by fast streaming of cosmic ray protons (Enßlin et al. 2011), it is unclear whether this mechanism can work when physics of the ICM is fully considered (see e.g. Wiener et al. 2013; Pinzke et al. 2017). Conversely, even the re-acceleration scenario needs seed electrons, which are usually originated by hadronic interactions (see e.g. Brunetti et al. 2017), to operate. Moreover, radio haloes are not present in all clusters. Observations suggest that the detection probability increases with the X-ray luminosity of the host cluster. At  $z \lesssim 0.2$ , radio haloes are found in about 30 – 35 per cent of galaxy clusters with an X-ray luminosity above  $\approx 1.3 \times 10^{45}$  erg s $^{-1}$  (Giovannini et al. 1999). It is unclear whether this is the result of insufficient sensitivity of current radio observations, or reflects a more profound reason linked to the physics of the ICM.

Indeed, only about 50 objects are known to host radio haloes (see Feretti et al. 2012, for a review and Giacintucci et al. 2017 for a reasonably updated census of mini haloes). All-sky surveys have been instrumental to the study of diffuse radio emission from clusters, as for instance the VLA NVSS survey (Condon et al. 1998). This survey mapped all radio sky above  $-40$  deg declination (almost 82 per cent of the sky) at 1.4 GHz, with a resolution of 45 arcsec (FWHM) and an rms sensitivity of  $\approx 0.45$  mJy beam $^{-1}$ . Although it was not primarily designed to detect radio haloes in

galaxy clusters, it laid the foundation to their study (Giovannini et al. 1999) by triggering follow-up campaigns, also employing other radio-telescopes, trying to extend the known sample both in number and in redshift (Venturi et al. 2007, 2008; Giacintucci 2011).

In the near future, the number of radio haloes in galaxy clusters is expected to increase thanks to the next generation of radio instruments, with observation targeted at detecting such diffuse structures. For example, one of the main science goals of the LOFAR Survey Key Project is to detect thousands of diffuse radio sources in clusters out to  $z \sim 0.8$ , with more than 100 at redshift above  $z \gtrsim 0.6$ , other than studying already detected radio haloes in clusters in more detail (Rottgering 2010). This should be possible thanks to the increased sensitivity of 0.25 mJy beam $^{-1}$  and a resolution of 25 arcsec full width at half-maximum (FWHM) for an observing frequency of 120 MHz (Tier 1 Large Area Survey). Similar performance is expected for future SKA observations, with the predicted discovery of about  $\sim 2500$  radio haloes up to  $z \sim 0.6$ , and probing a cluster mass range down to  $10^{14} M_{\odot}$ , which is not explored with current observations (Cassano et al. 2015). The sensitivity (0.02 mJy beam $^{-1}$ ) and resolution (10 arcsec FWHM) at 120 MHz are superior to those of the current generation of radio instruments.

The challenge for any successful picture trying to explain galaxy formation, and in particular the assembly of galaxy clusters, is therefore to properly model and predict the salient features of this extended radio emission. To this end, reproducing the scaling relations that link the radio halo power with structural properties of the halo, such as the virial mass (Cassano et al. 2013), or the ICM, such as the total X-ray power (Giovannini et al. 2009), give important insights into the diffuse radio emission phenomenology in clusters, other than being an important test bed for any galaxy formation and galaxy cluster physics theory.

Cosmological magnetohydrodynamics (MHD) simulations represent the most complete approach to investigate the complex interplay between magnetic fields and structures in the Universe. Performing those calculations from first principles, although desirable, still appears to be a remote goal given the tremendous dynamic range of spatial scales to be simultaneously modelled and the current uncertainties in our knowledge of baryon processes relevant for galaxy formation. Notwithstanding the advancement in the field (e.g. Dolag et al. 2016; Marinacci et al. 2015; Marinacci & Vogelsberger 2016), many of the cosmological MHD calculations performed so far do not include baryonic processes that are currently thought to play an essential role in galaxy formation and/or study the large-scale distribution of the field (Vazza et al. 2014b, 2015).

Although there exist examples of simulations studying diffuse radio emission in galaxy clusters with different techniques to model relativistic particles (see e.g. Dolag & Enßlin 2000; Xu et al. 2012), they are limited by several factors. Most importantly the great majority of the baryonic physics relevant for galaxy formation, and which has a non-negligible impact in setting the present-day strength of magnetic fields (see e.g. Marinacci et al. 2015), is largely ignored. Another limitation is that to reach high resolution, these calculations use the so-called zoom-in technique (Hahn & Abel 2011), simulating one object at a time. For instance, ZuHone et al. (2015) simulate the emergence of a radio mini halo by following the evolution and transport of cosmic rays, through passive tracer particles, in a simulation of cluster formation. While they include a detailed model for the cosmic rays evolution, the cosmological context is missing, together with physics of galaxy forma-



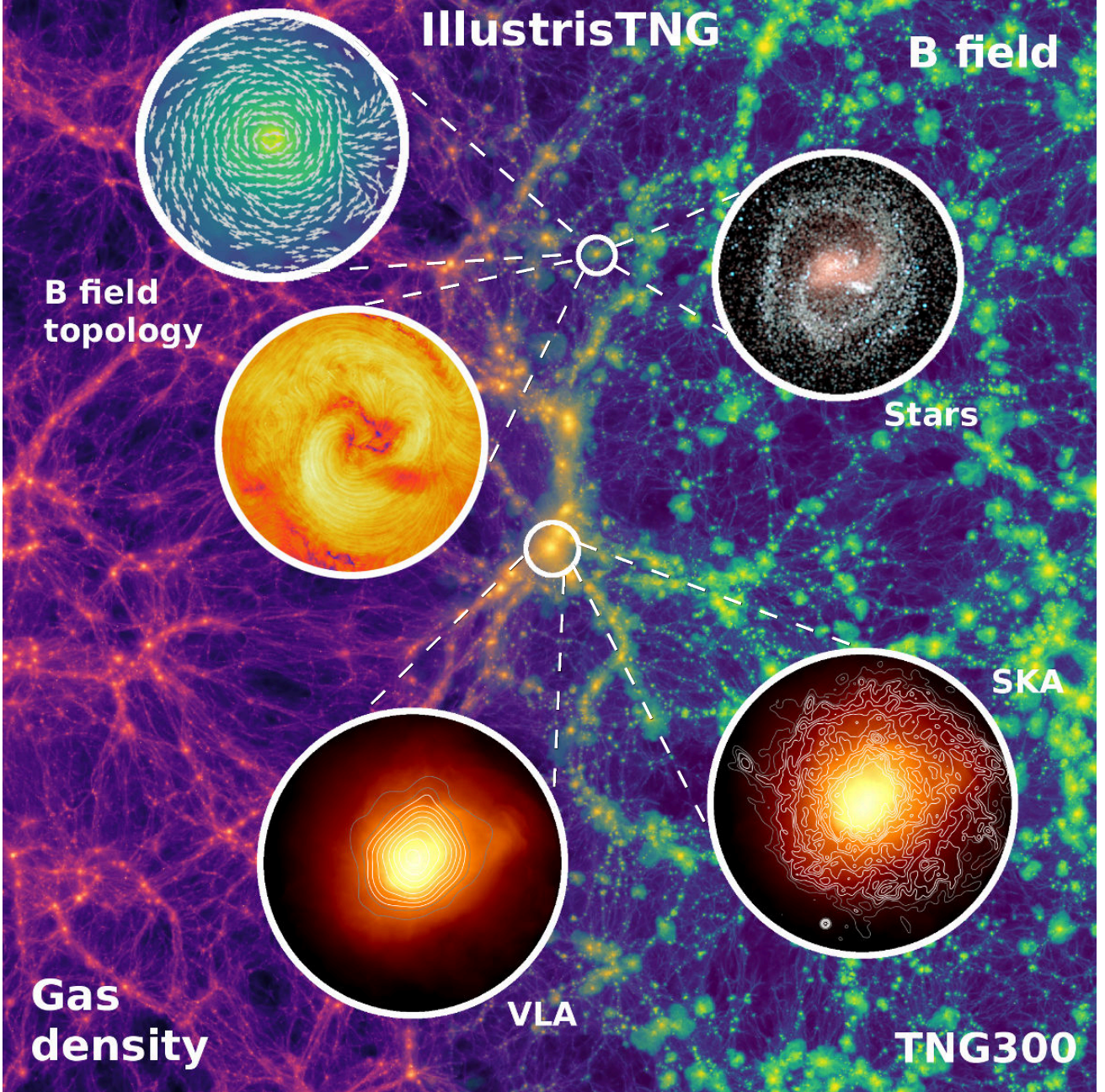


**Figure 1.** Gas column density map (left-hand side) and density-weighted projection of the magnetic field intensity (right-hand side) for the TNG300 box at  $z = 0$ . The projection extends for the full size of the TNG300 box ( $\approx 300$  Mpc) for a thickness of  $\approx 22.13$  Mpc and is centred on the most massive galaxy cluster. The zoomed panels on this structure show the X-ray emission (colours) overlaid with the extended ( $\sim 1$  Mpc) radio emission as seen with two different instruments. The zoomed panels on the small object illustrate the link between the magnetic field topology within a galaxy (on scales  $\sim 10$  kpc) and the galaxy morphology.

tion. [Donnert et al. \(2013\)](#) studied radio halo emission in an idealized MHD simulation of a merging galaxy cluster with cosmic ray transport, again with the same limitations. Moreover, most of the theoretical work has focused recently on studying the acceleration of particles to relativistic speeds in the ICM, an essential ingredient in synchrotron radio emission, with different levels of sophistication ([Pinzke et al. 2013](#); [Vazza et al. 2014a, 2016](#); [Wittor et al. 2016](#)). Therefore, in the study of radio haloes the superior statistical power that uniformly sampled magnetohydrodynamical cosmological simulations, which evolve magnetic fields (the other

key ingredient for synchrotron emission) self-consistently and include the most important baryonic physics processes in galaxy formation, can offer is paramount to make decisive steps forward in our theoretical understanding.

In this paper we extend previous work based on cosmological simulations by analysing the general magnetic field properties and the diffuse radio halo emission in galaxy clusters in the IllustrisTNG project, a set of cosmological magnetohydrodynamics simulations run with the moving-mesh code AREPO ([Springel 2010](#)) that include a comprehensive module for galaxy formation physics.

Simulation name	Realization	$L$ [ $h^{-1}$ Mpc]	$N_{\text{DM}}$	$N_{\text{gas}}$	$m_{\text{DM}}$ [ $h^{-1}M_{\odot}$ ]	$m_{\text{b}}$ [ $h^{-1}M_{\odot}$ ]	$\epsilon_{\text{DM},*}$ [ $h^{-1}$ kpc]	$\epsilon_{\text{gas}}$ [ $h^{-1}$ kpc]
<b>TNG300</b>	TNG300(-1)	205	2500 <sup>3</sup>	2500 <sup>3</sup>	$3.98 \times 10^7$	$7.44 \times 10^6$	1.0	0.25
	TNG300-2	205	1250 <sup>3</sup>	1250 <sup>3</sup>	$3.19 \times 10^8$	$5.95 \times 10^7$	2.0	0.5
	TNG300-3	205	625 <sup>3</sup>	625 <sup>3</sup>	$2.55 \times 10^9$	$4.76 \times 10^8$	4.0	1.0
	TNG300-DM-1	205	2500 <sup>3</sup>		$4.73 \times 10^7$		1.0	
	TNG300-DM-2	205	1250 <sup>3</sup>		$3.78 \times 10^8$		2.0	
	TNG300-DM-3	205	625 <sup>3</sup>		$3.03 \times 10^9$		4.0	
<b>TNG100</b>	TNG100(-1)	75	1820 <sup>3</sup>	1820 <sup>3</sup>	$5.06 \times 10^6$	$9.44 \times 10^5$	0.5	0.125
	TNG100-2	75	910 <sup>3</sup>	910 <sup>3</sup>	$4.04 \times 10^7$	$7.55 \times 10^6$	1.0	0.25
	TNG100-3	75	455 <sup>3</sup>	455 <sup>3</sup>	$3.24 \times 10^8$	$6.04 \times 10^7$	2.0	0.5
	TNG100-DM-1	75	1820 <sup>3</sup>		$6.00 \times 10^6$		0.5	
	TNG100-DM-2	75	910 <sup>3</sup>		$4.80 \times 10^7$		1.0	
	TNG100-DM-3	75	455 <sup>3</sup>		$3.84 \times 10^8$		2.0	

**Table 1.** IllustrisTNG contains three simulations covering three volumes, roughly  $\sim 50^3, 100^3, 300^3 \text{ Mpc}^3$ : **TNG50** ( $N_{\text{gas}} + N_{\text{DM}} = 2 \times 2160^3$ ,  $m_{\text{b}} = 5.74 \times 10^4 h^{-1} M_{\odot}$ ), **TNG100** ( $N_{\text{gas}} + N_{\text{DM}} = 2 \times 1820^3$ ,  $m_{\text{b}} = 9.44 \times 10^5 h^{-1} M_{\odot}$ ), and **TNG300** ( $N_{\text{gas}} + N_{\text{DM}} = 2 \times 2500^3$ ,  $m_{\text{b}} = 7.44 \times 10^6 h^{-1} M_{\odot}$ ). Here we use TNG100 and TNG300, ideally suited for cluster studies, and list the numerical parameters in the table. For each simulated box, we have performed simulations at three different resolution levels indicated by the numbers appended to the realization name (larger numbers denote progressively coarser resolution). Each level is spaced by a factor of 8 in mass resolution and a factor of 2 in softening length. For all runs we indicate the box side length ( $L$ ), the number of collisionless DM particles ( $N_{\text{DM}}$ ), and the initial number of gas cells ( $N_{\text{gas}}$ ) employed. We also report the masses of the DM particles ( $m_{\text{DM}}$ ) and of the baryonic component ( $m_{\text{b}}$ ). The gravitational softening lengths  $\epsilon_{\text{DM},*}$  indicate the maximum physical softening length (reached at  $z < 1$ ) of dark matter and star particles;  $\epsilon_{\text{gas}}$  is the minimum comoving value for the gravitational softening length of gas cells.

The main and novel aspect of our work is the analysis of the diffuse radio emission resulting from radio haloes in galaxy clusters (Feretti & Giovannini 1996; Feretti et al. 2012; Murgia et al. 2009; Vacca et al. 2011). We investigate radio emission from clusters by a detailed comparison with observations, trying to match the current observational constraints and to make predictions for the upcoming radio surveys that will be performed with the new generation of radio instruments such as SKA and LOFAR. The analysis of simulated radio haloes gives us a complementary view on the spatial extent and energy content of magnetic fields in galaxy clusters, since the radio emission is proportional to their strength. As such, the study of radio halo scaling relations (Giovannini et al. 2009; Cassano et al. 2013; Zandanel et al. 2014) with the total X-ray power and halo mass may yield important information about the amplification mechanisms of magnetic fields in clusters and the level of turbulence in the ICM. The modelling of radio emission makes it also possible to study the transport of charged particles and their re-acceleration to relativistic speeds, and it constrains the probability of detecting extended radio-emitting structures in a statistical sample of realistic simulated clusters. The comparison of the simulated radio emission with actual observations might also be employed as a useful check for the implementation of the galaxy formation physics modules used to perform the simulations, although our modelling of relativistic particles is rather preliminary and might have a non-negligible impact on the results.

Figure 1 gives a visual overview of the analysis performed in this paper. In the background it shows projected maps of gas density (left-hand side) and magnetic field intensity (right-hand side) in the TNG300 box (see Section 2 for details on this simulation) centred on the most massive galaxy cluster. The correlation between the large-scale magnetic field and the large-scale structure of the Universe appears evident. The zoom panels illustrate the aspects that we are going to analyse on individual haloes, namely the connection between magnetic fields and radio emission in galaxy clusters (on scales of  $\sim 1 \text{ Mpc}$ ) and the link between the properties of the magnetic field (on scales of  $\sim 10 \text{ kpc}$ ) and those of the hosting galaxies.

The paper is organized as follows. In Section 2 we briefly describe the IllustrisTNG simulation series and the numerical methodology. In Section 3 we present the general properties of magnetic fields in the IllustrisTNG series, both on large and on halo/galactic scales. In Section 4 we analyse the extended emission from radio haloes in galaxy clusters and their observational scaling relations to get further insights on the properties of magnetic fields in the simulations. Finally, Section 5 summarizes our findings. The modelling of radio and X-ray emission for galaxy clusters that we have adopted in this work is presented in Appendixes A–C.

## 2 THE ILLUSTRISTNG SIMULATION SERIES

The IllustrisTNG<sup>1</sup> simulation series is the follow-up project of the Illustris simulation suite (Vogelsberger et al. 2014a,b; Genel et al. 2014; Nelson et al. 2015; Sijacki et al. 2015). IllustrisTNG is comprised of a set of cosmological MHD simulations that follow a  $\Lambda$  cold dark matter cosmology with parameters  $\Omega_{\text{m}} = \Omega_{\text{dm}} + \Omega_{\text{b}} = 0.3089$ ,  $\Omega_{\text{b}} = 0.0486$ ,  $\Omega_{\Lambda} = 0.6911$ , Hubble constant  $H_0 = 100 h \text{ km s}^{-1} \text{ Mpc}^{-1} = 67.74 \text{ km s}^{-1} \text{ Mpc}^{-1}$ , and power spectrum normalization and index  $\sigma_8 = 0.8159$  and  $n_s = 0.9667$  (Planck Collaboration XIII 2016).

IllustrisTNG consists of *three* primary simulations: TNG50, TNG100, and TNG300. The side length of **TNG100** is  $L \simeq 100 \text{ Mpc}$  and its mass resolution is  $7.46 \times 10^6 M_{\odot}$  and  $1.39 \times 10^6 M_{\odot}$  for the dark matter (DM) and baryonic components, respectively. The adopted values for the gravitational softening lengths are  $\simeq 0.7 \text{ kpc}$  for DM and star particles (maximum physical value below  $z = 1$ ), while an adaptive comoving softening is used for gas cells with a minimum value of  $\sim 0.18 \text{ kpc}$ . The larger box, **TNG300**, has a side length of  $L \simeq 300 \text{ Mpc}$  and a mass resolution of  $5.88 \times 10^7 M_{\odot}$  and  $1.1 \times 10^7 M_{\odot}$  for the DM and baryonic components, respectively. The softening lengths are a factor of two larger than in

<sup>1</sup> <http://www.tng-project.org>



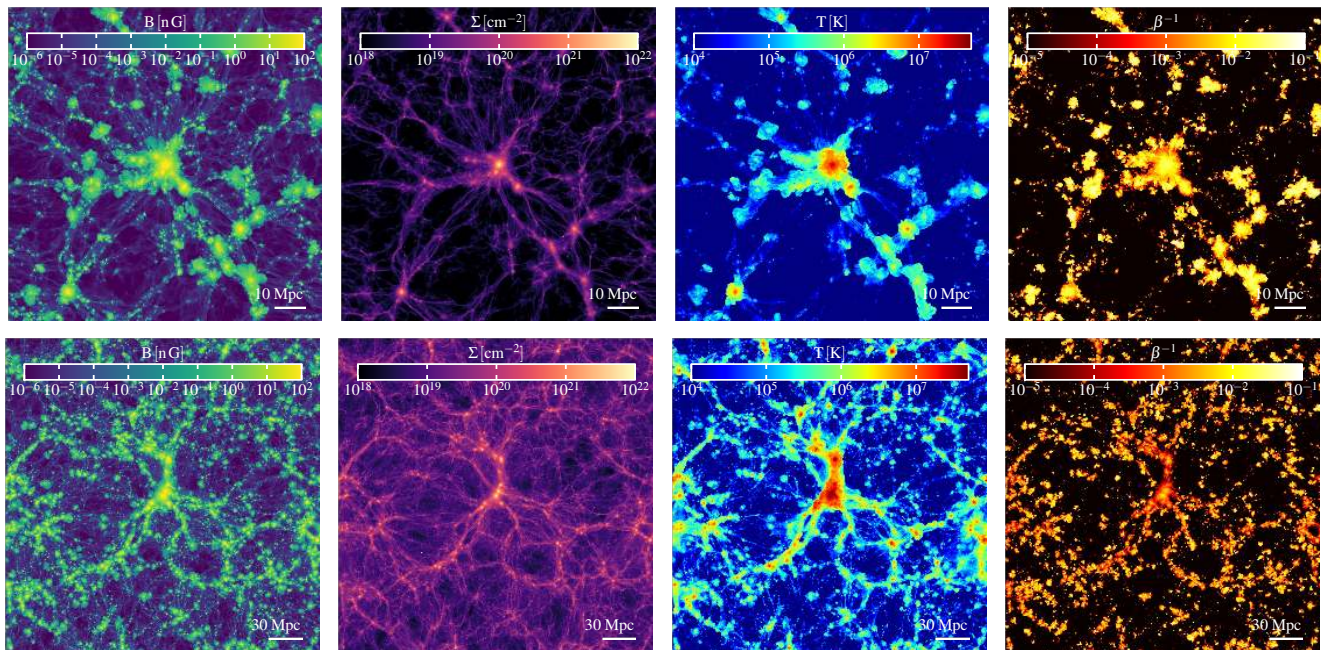


**Figure 2.** Top row (from left-hand to right-hand side): Density-weighted projection of the magnetic field intensity, gas column density map, projected mass-weighted gas temperature and projected ratio between magnetic and thermal pressure at redshift zero for the TNG100 simulation. The centre of the projection region corresponds to the location of the most massive halo in the box and a slice of  $\approx 100$  Mpc on a side and  $\approx 7.38$  Mpc in depth is shown. Bottom row: Corresponding plots for TNG300 with a side length of  $\approx 300$  Mpc and a thickness of  $\approx 22.13$  Mpc.

the TNG100 case. The smaller box, **TNG50**, has a side length of  $L \approx 50$  Mpc and a mass resolution of  $4.43 \times 10^5 M_\odot$  for DM and  $8.48 \times 10^4 M_\odot$  for baryons. The softening lengths adopted are  $\approx 0.3$  kpc for collisionless particles (maximum physical value below  $z = 1$ ), and a minimum comoving softening of  $\approx 0.07$  kpc for gas cells. All the reported values refer to the highest resolution realizations of each box. In this work, we will present only results obtained from the TNG100 and TNG300 series at the resolution quoted above since we are focusing on massive haloes.

For all the runs two additional simulations at lower resolution are also performed. Each resolution level differs from the other in terms of mass resolution and in the values of the softening lengths: in passing to a lower resolution level mass resolution is degraded by a factor of 8 and, accordingly, softening lengths are increased by a factor of 2. Finally, we have also run the associated DM-only simulations for all resolution levels. The primary numerical parameters of each realization can be found in Table 1.

The simulations are carried out with the moving-mesh code AREPO (Springel 2010). The IllustrisTNG simulations employ a comprehensive module for galaxy formation physics, which is an updated version of the Illustris model (Vogelsberger et al. 2013). The updated model is described in Weinberger et al. (2017) and Pillepich et al. (2018a) to which we refer the reader for more details. The principal differences with respect to Illustris are: a new radio mode AGN feedback model (Weinberger et al. 2017), a revised SN wind model and refinements in the chemical evolution (Pillepich et al. 2018a), and the addition of ideal MHD (Pakmor et al. 2011; Pakmor & Springel 2013) with a Powell et al. (1999) eight-wave divergence cleaning approach that yields results of comparable quality to the ones obtained with constrained transport schemes (Evans & Hawley 1988) by keeping divergence errors under control (see again Pakmor & Springel 2013). Furthermore, several algorithmic advances in the AREPO code have been employed

in the new simulation suite, such as the use of a more flexible hierarchical time integration for gravitational interactions (Springel et al., in preparation) and improvements of the convergence rate of the underlying (magneto-)hydrodynamical solver (Pakmor et al. 2016). In IllustrisTNG the code evolves the MHD equations starting from a homogeneous magnetic field of  $10^{-14}$  (comoving) Gauss. In previous work (e.g. Marinacci et al. 2015; Marinacci & Vogelsberger 2016; Pakmor et al. 2014, 2017) we have shown that the final outcome is insensitive to the actual value of the seed field over several orders of magnitude.

This work is part of a series of five papers introducing the IllustrisTNG project. Each one of these papers investigates different topics of the new simulations in order to illustrate their full scientific potential. In particular, in this paper we investigate the properties of the magnetic fields and diffuse radio emission in galaxy clusters. In Pillepich et al. (2018b), we study the stellar content and distribution in massive haloes. In Nelson et al. (2018), we show the colour distribution of the simulated galaxies and compare it with SDSS observational constraints. In Springel et al. (2018), we examine the galaxy and matter clustering signal in the simulations and compare it with observations at low and high redshift. Finally, Naiman et al. (2018) explore different channels for metal enrichment in the simulations, focusing on chemical elements, such as europium, produced by r-processes in neutron star–neutron star mergers.

### 3 MAGNETIC FIELD STATISTICS

We start our analysis of the magnetic field properties in the IllustrisTNG simulations by discussing statistics of the fields at large cosmological and at halo/individual galaxy scales.

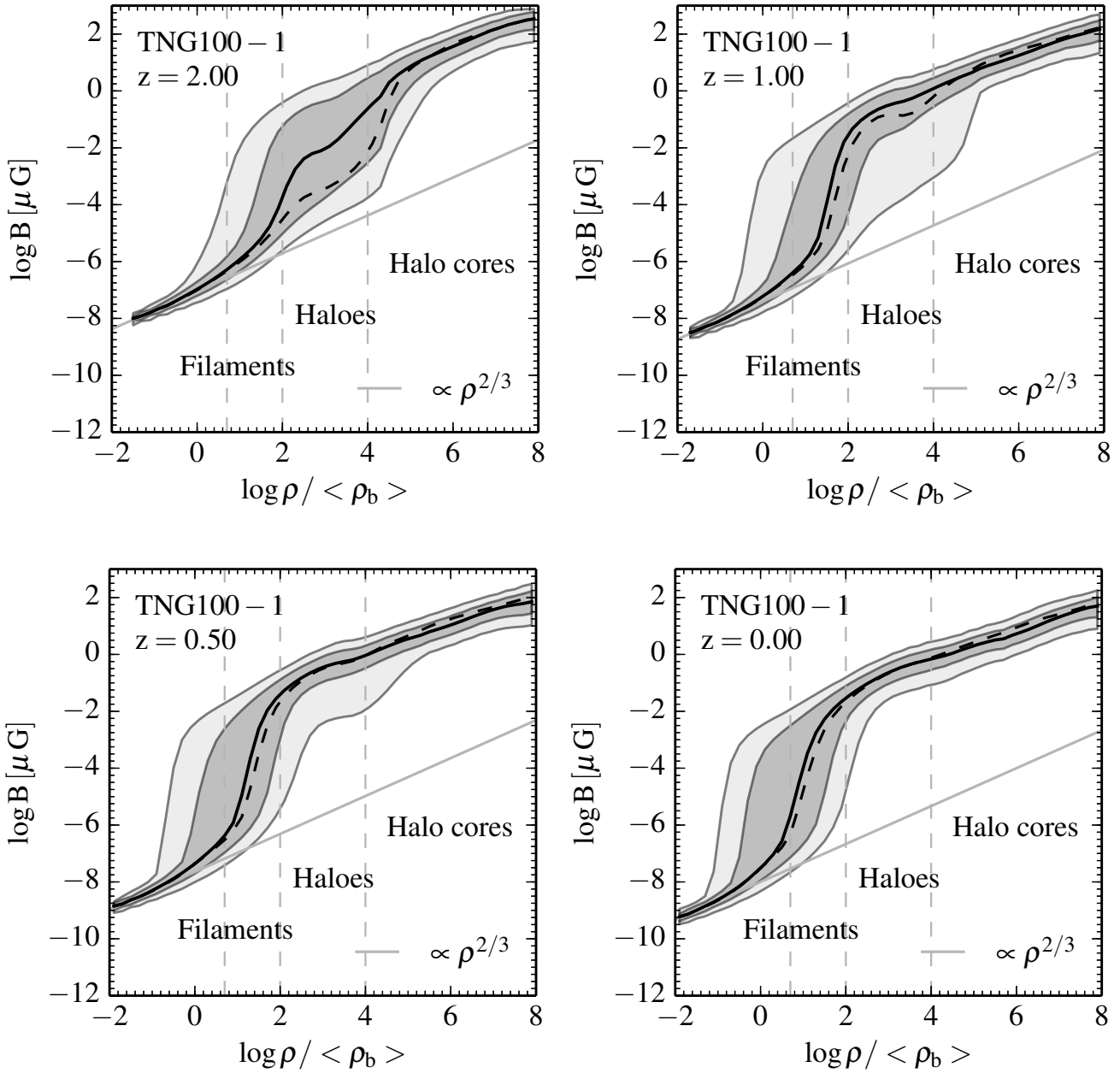


**Figure 3.** Redshift evolution of the magnetic field intensity versus baryon overdensity for the simulation TNG100. The black solid lines represent the median of the magnetic field distribution while the corresponding shaded areas indicate the  $1\sigma$  (dark grey) and  $2\sigma$  (light grey) spread around the median relation. We also show the density scaling of the magnetic field intensity ( $\propto \rho^{2/3}$ ) expected in case of magnetic flux conservation (grey solid lines). At late times it is clearly visible how the amplification of the magnetic field is driven by the assembly of cosmic structures and enhanced by radiative cooling and feedback processes. In particular, at low overdensities [ $\log(\rho/\rho_b) \sim 0$ ] the median relationship follows closely the expected scaling for magnetic flux conservation but then steepens and forms a second branch at magnetic field intensities that are four to five orders of magnitude larger than this expectation at large [ $\log(\rho/\rho_b) \gtrsim 1$ ] overdensities. The drop of the magnetic field values [ $\propto (1+z)^2$ ] is again the effect of magnetic flux conservation and caused by the cosmological expansion. In all panels, the dashed black line represents the median trend obtained for the TNG300 box.

### 3.1 Large-scale statistics

In Fig. 2, we present projections of a thick slice for the TNG100 (top row) and TNG300 (bottom row) runs, respectively. For each simulation four panels are displayed. From left to right they are: density-weighted projection of the magnetic field, gas column density map, mass-weighted gas temperature projection, and projected

ratio between magnetic and thermal pressure ( $\beta^{-1}$ ) of the gas. For both simulations, all the projections are centred on the most massive halo and show the full box size on the projection plane with a projection depth equal to  $5 h^{-1} \text{Mpc}$  and  $15 h^{-1} \text{Mpc}$  for TNG100 and TNG300, respectively.

The projections give a qualitative view of the large-scale distribution of the magnetic field in the simulations. We note that the



main properties of the magnetic field on large scales (strength and spatial coincidence with haloes) are basically independent of the size of the simulated volume, even though the TNG300 run has a mass resolution of a factor of eight worse than the TNG100 box. Indeed, from Fig. 3 we see that  $\|B\|$  as a function of the baryon overdensity differs by at most a factor of 0.25 dex between TNG100 and TNG300 inside halo cores.

By comparing the projections of the magnetic field strength and gas density, it is apparent that the highest values of the field are found at the highest density peaks. This is in line with what has been reported in Marinacci et al. (2015, and references therein), who found that magnetic fields are largely amplified from the initial seed value within haloes by the combined action of shear flows and turbulence induced by structure formation and stellar and AGN feedback processes. Differently from Marinacci et al. (2015), the distribution of the magnetic fields tracks more closely the density distribution of gas. This is due to the difference in the implementation of the AGN feedback model (see Weinberger et al. 2017), which is less bursty in the IllustrisTNG simulations compared to the original Illustris model used in Marinacci et al. (2015). This is also apparent by comparing the temperature projections. In IllustrisTNG the high temperature regions are only found within massive haloes, while due to the radio mode feedback implementation in Illustris (see Sijacki et al. 2007; Vogelsberger et al. 2013) those regions extend much further out. The ratio between magnetic and gas thermal pressure shows that the highest values are reached around density peaks within haloes while they drop dramatically in filaments and voids. The largest  $\beta^{-1}$  values are achieved in low-mass haloes, with the central value of  $\beta^{-1}$  is declining with increasing virial mass for both boxes (see also discussion of Fig. 6). This is due to the larger gas temperatures in massive haloes that tend to decrease the maximum value of  $\beta^{-1}$ . In TNG300 the coarser resolution also plays a role because the B field amplification is somewhat reduced. Generally, magnetic fields are dynamically unimportant on large scales.

In Fig. 3, inspired by Dolag et al. (2005), we show more quantitatively the redshift evolution of the magnetic field intensity as a function of the baryon overdensity for TNG100. Vertical dashed lines roughly separate regions such as filaments, haloes and halo cores at selected values of baryon overdensities. The solid grey line indicates the expected scaling under the assumption of magnetic flux conservation. The solid black line shows the median trend of magnetic field intensity, while the shaded areas indicate the  $1\sigma$  (dark grey) and the  $2\sigma$  (light grey) dispersion around the median value.

At all redshifts, it can be seen that the amplification of magnetic fields from their seed value is driven by the assembly of structures. At low baryon overdensities, the magnetic field strength follows the relation expected from magnetic flux conservation arguments, i.e. the amplification is primarily driven by the compression of the gas. This trend changes dramatically for overdensities above  $\approx 10$  where a sudden increase of the field strength sets in, up to about four or five orders of magnitude above the flux conservation predictions. This is indicative that additional processes – e.g. shear flows and turbulence (see also Dolag et al. 1999, 2002) – are at play to amplify magnetic fields. The field strength after the sudden increase at overdensities  $\sim 10$  keeps increasing with baryon overdensity. Trends are similar at all redshift, with the  $z = 2$  panel showing the least abrupt change in magnetic field intensities from low to high overdensities. However, even at  $z = 2$  most of the amplification at large overdensities has already occurred. We also find the same trends (shown by the dashed black lines in Fig. 3)

for the TNG300 box. Given the lower resolution of this run, the magnetic field amplification is less pronounced at the transition region between low-density gas and gas within haloes (especially at  $z = 2$ ). However, at low and large overdensities the predictions of the TNG100 and TNG300 simulations agree. To conclude, given the similarity in the shape of the median magnetic field strength-gas overdensity relation with the one found by Marinacci et al. (2015) in their full-physics simulations, we would like to point out that the full spectrum of baryon physics, and in particular the presence of feedback loops, is needed to amplify the initial seed field to values of  $\sim 10\mu\text{G}$  observationally found inside galaxies (see also Section 3.2).

### 3.2 Halo and galaxy statistics

We investigate the connection between galaxy morphology and magnetic field topology in Figs. 4 and 5, where we select three examples of early-type galaxies (Fig. 4) and late-type galaxies (Fig. 5) from the TNG100 simulation. For each galaxy class, the three columns show from left to right: stellar density, gas density and volume-weighted magnetic field intensity. In the two latter columns, superimposed arrows show the direction of the velocity and magnetic fields, respectively.

Early-type galaxies show predominantly a spheroidal distribution of stars and a highly irregular gas distribution, which is due to the interaction of the AGN kinetic feedback with the surrounding gas (see also Gaspari et al. 2012; Weinberger et al. 2017). An exception is represented by the least massive galaxy of the sample, in which a thick and old stellar disc and a more regular spheroidal gas distribution are present. The magnetic field intensity traces the gas density distribution very closely and its topology is highly irregular. Magnetic field lines tend to prevalently orient along the gas filaments visible in the projections, which, in the second case, also correlate with the predominant direction of the velocity field presented in the middle panel.

For late-type galaxies stars are organized in a comparatively thin disc with respect to the early-type galaxies. The disc still shows residual star formation, as the blue stellar colours indicate. The gas is also organized in a similar structure, which is rotationally supported and extends far beyond the stellar disc of the galaxy, as the density projection panels clearly show. For the first galaxy presented here the bipolar configuration of the galactic wind generated by stellar feedback is also visible in the edge-on gas projection. The magnetic field intensity follows closely the gas distribution. However, the most striking difference compared to early-type galaxies is that the topology of the field is much more regular and the field is predominantly oriented with the gaseous disc. In fact, within discs the magnetic field is mostly toroidal and anti-aligned with the direction of the velocity field. We would like to note that the magnetic field orientation could switch back and forth between aligned and anti-aligned configurations (see also Pakmor et al. 2014). Moreover, the differential rotation of the gaseous disc can provide the source for field amplification via a galactic dynamo (see also Pakmor et al. 2017), although it is unclear if this can be directly modelled at the resolution achieved in IllustrisTNG. The final magnetic field intensities ( $\approx 1 - 10\mu\text{G}$ ) are consistent with observational findings for late-type galaxies (Basu & Roy 2013; Beck et al. 1996; Beck 2009, 2015).

In Fig. 6, we show stacked profiles of the mass-weighted magnetic field intensities (top six panels) and the ratio between magnetic and thermal pressure (bottom six panels). Solid lines in each panel show the median trend and dark and light shaded areas the

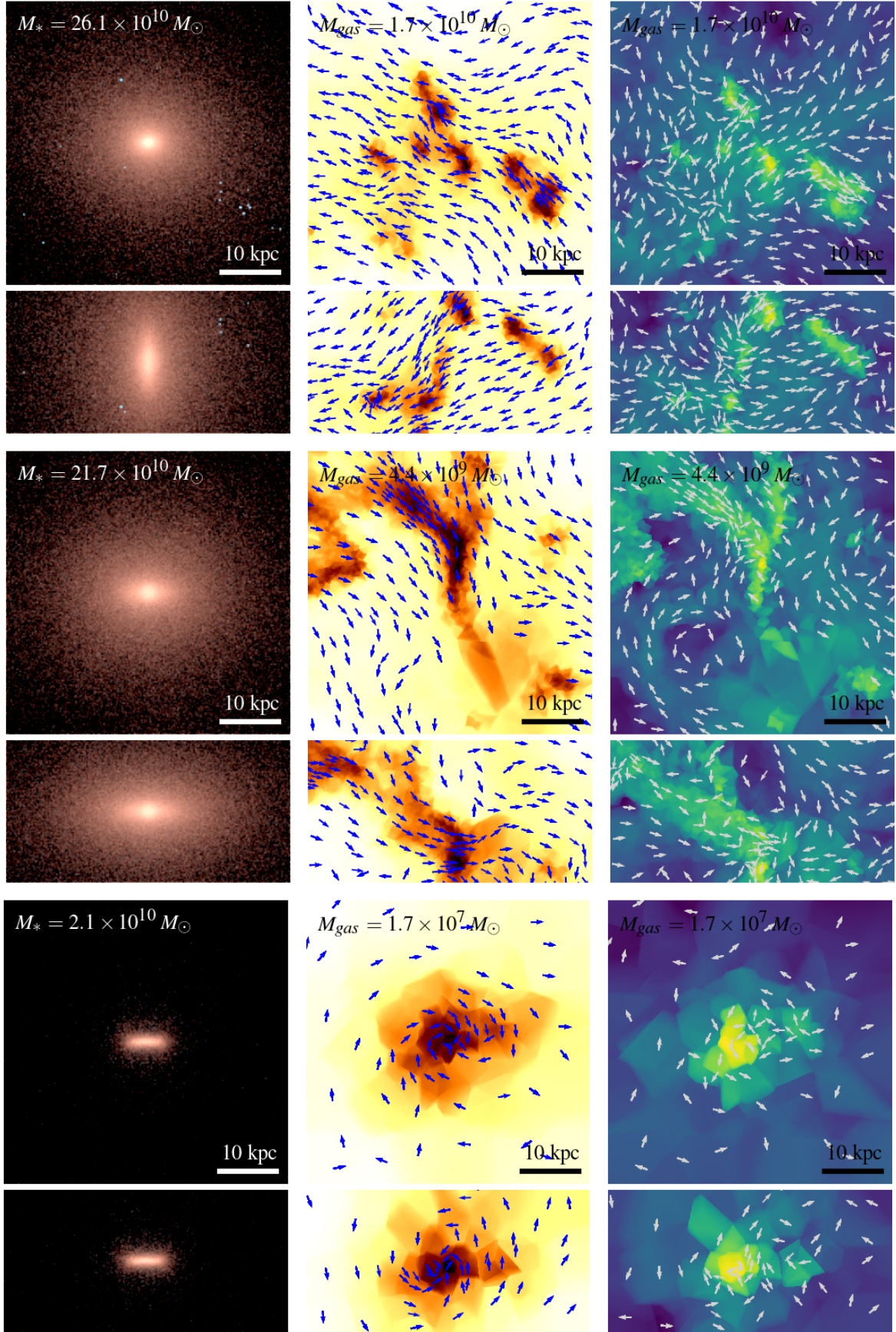


**Figure 4.** Stellar (left-hand panels), gas density (middle), and volume-weighted magnetic field (right-hand panels) projections of three early-type galaxies in the TNG100 simulation. The arrows show the direction of the velocity and magnetic fields in the gas density and magnetic field panels, respectively.



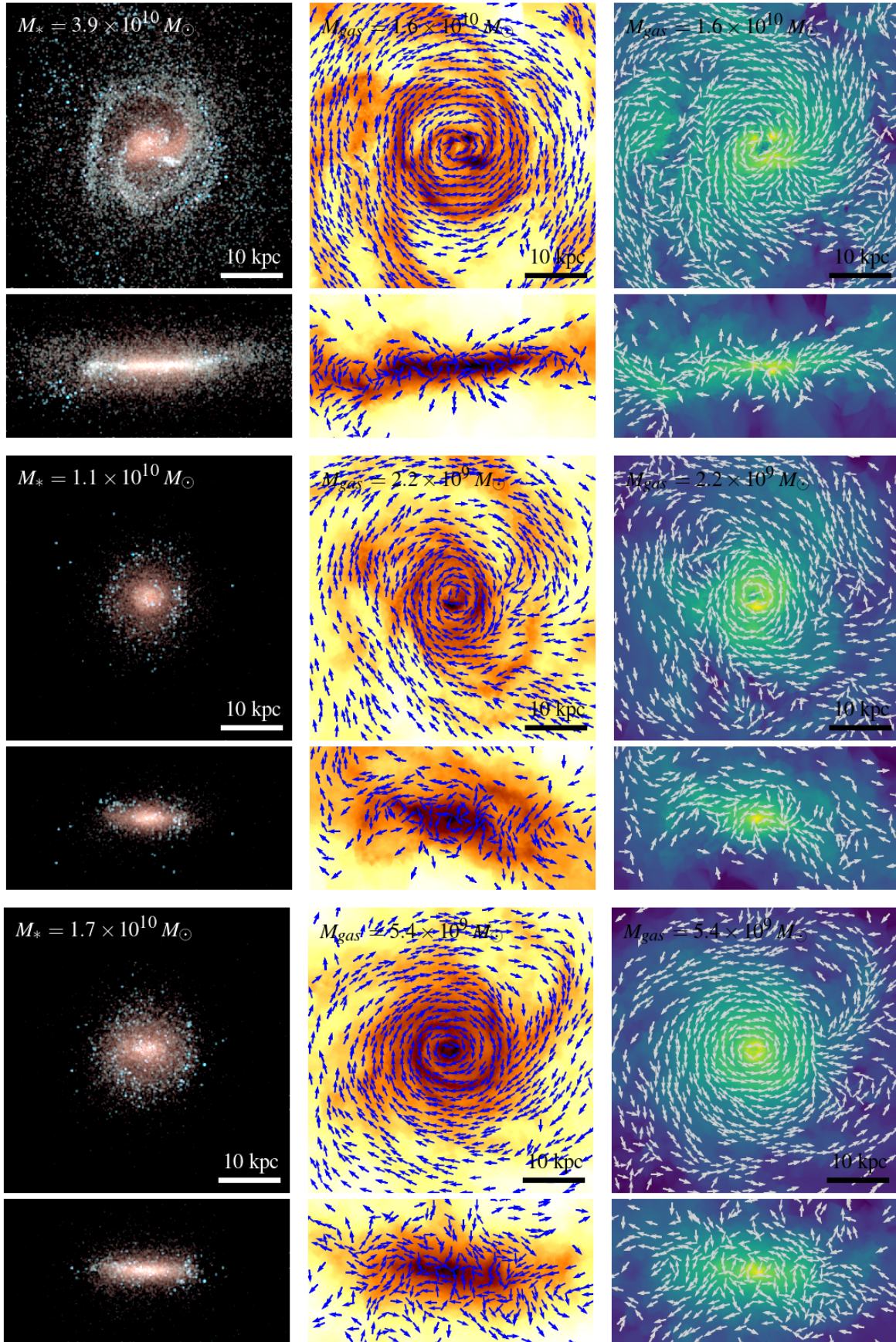


**Figure 5.** As in Fig. 4 but for three late-type galaxies in the TNG100 simulation.

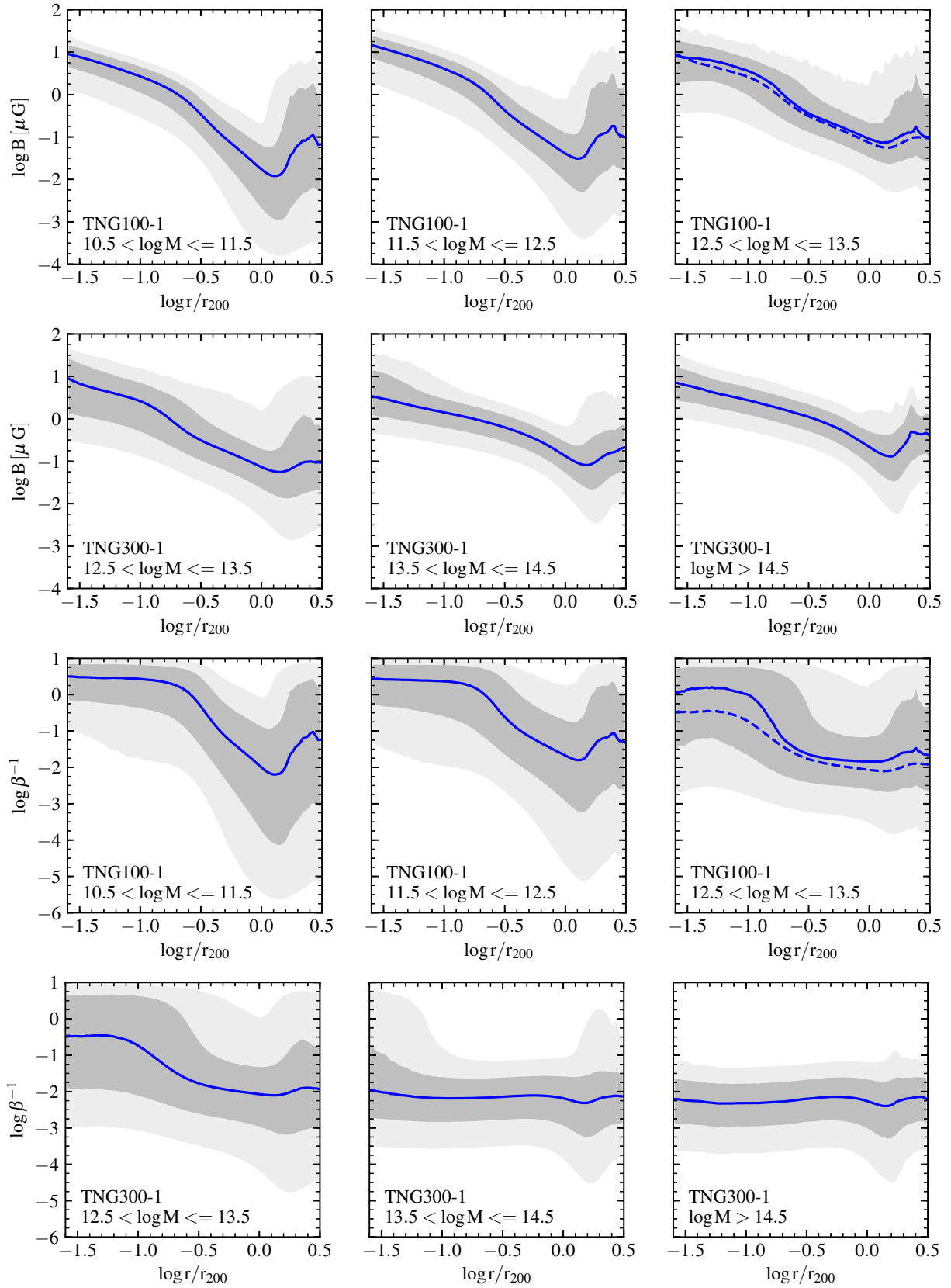


**Figure 6.** Top six panels: Radial magnetic field intensity profiles at redshift zero. The figure presents the stacked profiles of the FOF groups in the virial mass bins indicated in each panel. Less massive haloes have been taken from the TNG100 run (top row), while, at the more massive end, haloes from the TNG300 run (bottom row) have been used. The solid blue line represents the (mass-weighted) median trend while the dark and light grey regions show the  $1\sigma$  and  $2\sigma$  spread around the median value, respectively. Bottom six panels: Radial profiles of the ratio between magnetic and thermal gas pressures at redshift zero. To facilitate the comparison in the overlapping mass bins, we report the median relation for the TNG300 run in the TNG100 results as a blue dashed line.



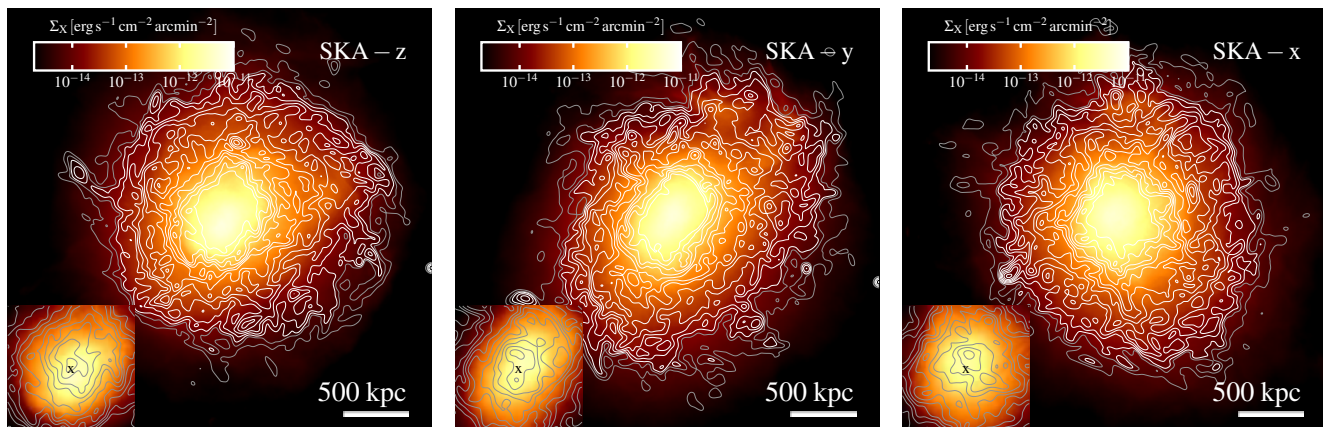


**Figure 7.** X-ray map (colour) overlaid with synchrotron emission contours (model 1 in Section A2) for the most massive halo of the TNG300 simulation taken from the  $z = 0$  snapshot. The panels are 3.5 Mpc on a side and in projection depth and show projections in the  $xy$ ,  $xz$ , and  $yz$  planes from left to right, respectively. Note how the X-ray and radio morphologies match one another, indicative of the fact that the gas and large-scale magnetic field morphologies are similar. Note also the offset between the centres of X-ray and radio emissions. X-ray maps are displayed to a minimum surface brightness value of  $1.95 \times 10^{-15} \text{ erg s}^{-1} \text{ cm}^{-2} \text{ arcmin}^{-2}$ , assuming a telescope effective area of  $200 \text{ cm}^2$  (Anderson & Bregman 2010). Radio maps are smoothed on a scale of 10 arcsec (FWHM) with a Gaussian kernel. Contour levels are placed at  $0.06 \text{ mJy beam}^{-1}$  spaced by a  $\sqrt{3}$  factor from one another (white, representing detections), while grey contours are at 0.02 and  $0.04 \text{ mJy beam}^{-1}$ . These values are representative of the typical beam size and sensitivity ( $0.02 \text{ mJy beam}^{-1}$  is the  $1\sigma$  noise level) of future SKA observations of radio haloes in galaxy clusters (see Vazza et al. 2015). The assumed redshift used to generate the X-ray and radio maps is 0.2. More details about map creation can be found in Appendix A and Table A1.

associated  $1\sigma$  and  $2\sigma$  spreads. Regardless of the halo mass bin<sup>2</sup>, the magnetic field intensity is a declining function of radius and is declining more slowly in more massive haloes. The intensity of the field tends to decline faster once a radial distance  $r \sim 0.3 r_{200}$  is reached. Past the virial radius, magnetic field intensities tend to increase again, which is due to the contribution of substructures. Magnetic field intensities in the centres are  $\approx 1 - 10 \mu\text{G}$  with a drop of about three orders of magnitude in the external regions. These values have to be compared with a magnetic field intensity of  $\approx 10^{-3} \mu\text{G}$  (i.e. the value of the seed field scaled by adiabatic compression at the highest baryon overdensities), which demonstrates the efficient amplification of the field within haloes due to structure formation. The maximum value reached by the magnetic field intensity is consistent across all mass bins. The TNG300 simulation shows in general good agreement, in both the central B field value and the slope of the relation, for the overlapping virial mass bins despite its coarser resolution when compared to TNG100 (see the blue dashed line for a direct comparison). If anything, the magnetic field profile in the overlapping mass bin declines slightly faster with radius, which is likely due to a less efficient amplification caused by numerical diffusion on the coarser grid scale (e.g. Cho & Ryu 2009; Jones et al. 2011; Vazza et al. 2014b).

The ratio between magnetic and thermal pressure ( $\beta^{-1}$ ) gives an indication of the importance of magnetic fields on the dynamics of the gas. From the bottom six panels in Fig. 6, it can be seen that in the external regions of the haloes, for distances  $\sim 0.3 r_{200}$ , magnetic fields are sub-dominant and the  $\beta^{-1}$  ratio is at most 0.1. Moving to the inner regions, the value of the field gets largely amplified by the combined action of radiative cooling (leading to high baryon overdensities) together with the increased level of shear and

turbulent gas motions triggered by stellar and AGN feedback (see also Marinacci et al. 2015), while the thermal content of the gas declines due to the efficient cooling occurring at the halo centres. It is currently unclear whether with the present resolution it is possible to model the emergence of a small-scale dynamo amplification (see e.g. Rieder & Teyssier 2017), although measurements of the turbulence spectra (Pakmor et al. 2017) in higher resolution cosmological simulations performed with AREPO are consistent with this scenario. Strong magnetic field amplification and effective gas cooling at the halo centres both contribute to increase the  $\beta^{-1}$  up to a value of  $\sim 3$ , as it is visible for the panels analysing the TNG100 run. Note also that in this case the contribution of the magnetic field to the dynamics of the gas is in general sub-dominant, since the magnetic pressure is typically smaller (of the order of  $\sim 30$  per cent) than the kinetic energy density content of the gas (see also Pakmor et al. 2017, for a calculation at higher resolution focusing on the Milky Way mass scale). For the panels showing the results of the TNG300 simulation, this increase of the  $\beta^{-1}$  ratio is also present, but the maximum value never exceeds a few percent or tens of percent. We ascribe this difference between TNG100 and TNG300 to two effects: the lower numerical resolution of the latter simulation, which yields lower or more rapidly declining values for B fields (note that the most massive bin of the TNG100 and the least massive bin of the TNG300 runs overlap; the two simulations can be directly compared here with the help of the blue dashed line); and the mass of the haloes analysed in the TNG300 runs that host high-temperature gas, which is kept hot by AGN feedback processes, in the halo regions.

#### 4 OBSERVATIONAL SIGNATURES IN MASSIVE HALOES

In this section we explore several mock observations and scaling relations that depend on magnetic fields within massive haloes. We

<sup>2</sup> Unless otherwise stated, halo masses (i.e. virial masses) are expressed in terms of 200 times the critical density for closure  $\rho_{\text{crit}} = 3H_0^2/(8\pi G)$  throughout the paper.

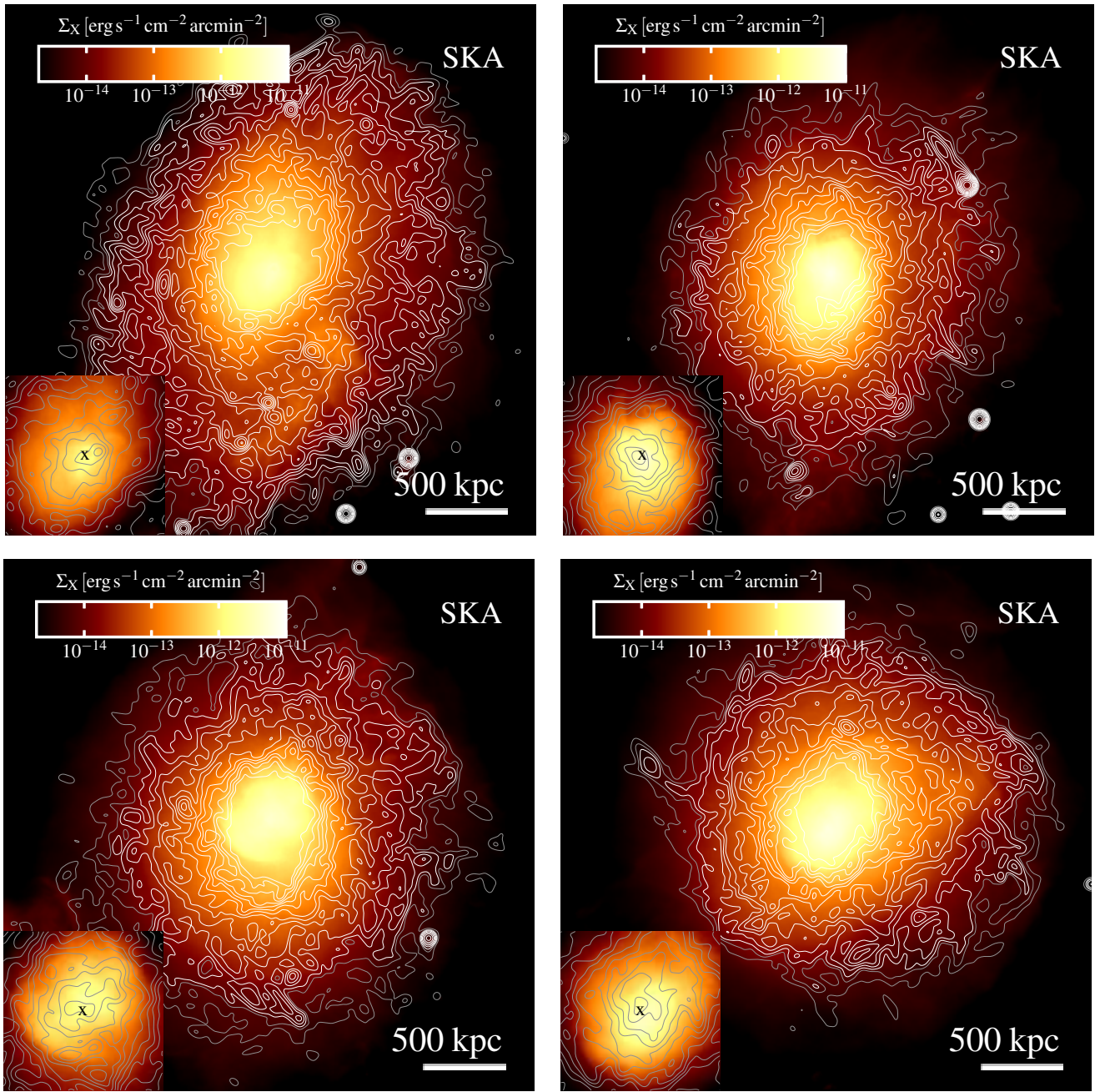


**Figure 8.** As in Fig. 7, but showing the evolution of the most massive halo. Note at earlier times the presence of compact regions of radio emission without any significant X-ray counterpart originating from substructures. Maps are generated for the  $z = 0.3$ ,  $z = 0.2$ ,  $z = 0.1$ , and  $z = 0$  (from top left to bottom right) outputs, respectively.

focus on the massive end of the TNG300 box by adopting a lower cut in virial mass of  $10^{14} M_{\odot}$ , which is below the value explored by current radio observations, but it will be probed by future SKA surveys (Cassano et al. 2015). This leaves us with a sample of 280 haloes in total. A description of how the X-ray and radio emission are modelled can be found in Appendices A and B. In particular, for radio halo emission we have compared two different models in our analysis. They differ in the way the distribution of relativistic particles (and in particular electrons) is parametrized and we refer the reader to Sections A2 and A3 for their complete characterization.

We would like to caution that the models for the relativistic electron distribution that we adopt in this analysis are rather simplistic. However, the scope of this work is not to find nor suggest a solution to all the outstanding issues related to the complex phenomenon of radio halo emission in galaxy clusters. Instead, with the present analysis we aim at exploiting the unique opportunity that the IllustrisTNG suite offers in terms of number of galaxy clusters simulated with a cutting-edge galaxy formation physics model that includes self-consistently the evolution of magnetic fields. To do so it is natural to first use simple models for the distribution of relativistic particles to explore them and assess their weak points



under the assumption that the magnetic field properties predicted by the simulations can be trusted. Trying more complex and advanced models for relativistic particles and comparing them in detail with the observations would be desirable, but it is outside the scope of the present investigation. The optimal solution would be to self-consistently include cosmic rays in the calculations (e.g. Pakmor et al. 2016; Pfrommer et al. 2017), but in large cosmological volumes, as the ones probed by IllustrisTNG, this is a very challenging numerical task that is still very far from a satisfactory solution.

#### 4.1 Radio and X-ray mock observations

Figure 7 shows a composite X-ray image overlaid with radio emission contours (see Appendix A for details on how X-ray and radio – model 1 in Section A2 – emissions are computed) for the most massive halo of the TNG300 simulation ( $M_{200} = 1.53 \times 10^{15} M_{\odot}$ ). This galaxy cluster would observationally be classified as having extended radio halo emission. The three panels show different projections (along the  $z$ ,  $y$ , and  $x$  axis). The inset on the bottom left-hand corner of each panel is 800 kpc across and shows a zoom of the central region. The inset is centred on the potential minimum of the halo, and the ‘x’ indicates the centre of the X-ray emission, which coincides with the centre of the projection. The colour map showing the X-ray brightness displays only values above the detection limit for typical *Chandra* parameters. Radio contours are placed at  $1\sigma$  and  $2\sigma$  rms level (grey, corresponding to non-detection) and at levels  $> 3\sigma$  spaced by factors of  $\sqrt{3}$  (white, corresponding to detection) and are computed for an SKA observation at 120 MHz, with the associated resolution and sensitivity (see Table A1). Only gas cells that are not eligible for star formation in our galaxy formation physics model (i.e. gas with  $n \lesssim 0.1 \text{ cm}^{-3}$ ) and that are cooling are considered for computing radio and X-ray emission. We apply this selection criterion in all the figures presenting radio and/or X-ray results.

The maps indicate that X-ray and radio emissions are spatially coincident. The morphology of both emission maps is regular and roughly spherical, although in the  $y$  projection both radio and X-ray emissions are elongated in the lower left to upper right direction. Radio contours follow quite closely the shape of the X-ray emission, showing the close link between the physics generating the two processes. In particular, X-rays probe the thermodynamic state of the hot gas, while radio emission probes the strength and amplification of the magnetic fields. Both the thermodynamics of the gas and the field strength are set by the assembly of the cluster and feedback processes due to AGN and stellar feedback. So a connection between these two emission mechanisms is expected.

However, by looking more closely at the central regions it can be seen that there is an offset between the radio and X-ray signals. This shift depends on the orientation chosen for the projection: for example, the two maxima of the emission are almost coincident in the left-hand panel, while the offset becomes more noticeable in the other two orientations. In the middle panel, the centre of the X-ray emission is in between two local maxima of the radio map. An offset between the maxima of X-ray and radio emissions is also often found in radio halo observations (Govoni et al. 2012). Radio haloes can be quite asymmetric and the offsets are more pronounced for more asymmetric distributions and smaller radio halo sizes (Feretti et al. 2010). A possible explanation for this offset can be the presence of large spatial variations in the intracluster magnetic field or a non-uniform distribution of relativistic particles. Note that our modelling does not include the latter effect, which implies that we might be underestimating the offsets in this analysis.

In Fig. 8, we present the evolution of the X-ray and radio (model 1 in Section A2) significant X-ray counterpart, originating from substructures, is also present. Consistent with the observations the X-ray/radio offset is more pronounced where the radio (and the X-ray) emission is more asymmetric. The offset between the X-ray and radio can be interpreted as the presence of magnetic field variations in the ICM likely caused by shear and turbulent gas motions – triggered by radiative cooling instabilities and stellar and AGN feedback, which may initiate a dynamo process – that contribute to the amplification of the magnetic field and are not necessarily coincident with the gas density peak where the bremsstrahlung mechanism is more efficient.

In Fig. 9, we show radio and X-ray maps of the 20 most massive haloes ( $M_{200} = 3.79 \times 10^{14} - 1.53 \times 10^{15} M_{\odot}$ ) in TNG300. These radio maps were generated by assuming model 1 (see Sec. A2) for the distribution of relativistic electrons and with parameters typical of VLA observations. Thus, their resolution is lower and their sensitivity smaller than the SKA maps shown before (see Table A1). Also, they probe higher frequency synchrotron radiation (at 1.4 GHz), and this, given the spectral form of the radiation that we have assumed ( $\propto \nu^{-1.7}$ ), implies a lower radiation flux at a fixed distance. We note that only these 20 massive haloes are presented because, with only a handful of exceptions, less massive objects have non-detectable extended radio emission with the typical VLA parameters that we have adopted to generate the radio maps. Indeed, only the five most massive galaxy clusters, out of 280 with virial mass above  $10^{14} M_{\odot}$ , would be detected as having extended radio haloes according to the criterion expressed in equation (2) below.

For the most massive haloes, the majority of the analysed objects presents a radio emission whose morphology matches the one of the X-ray emitting gas. The extent of the radio emitting region, however, varies on a halo by halo basis. We analyse this aspect in more detail in Section 4.2. Visually, it is also possible to distinguish two classes of radio haloes: (i) more extended ( $\gtrsim 1$  Mpc across) haloes with relatively low central surface brightness and (ii) more compact haloes ( $\lesssim 1$  Mpc across) with a much steeper radial profile and large central brightness. This division is reminiscent of the observational classification of giant radio haloes and mini haloes (Bravi et al. 2016; Cassano et al. 2008; Feretti & Giovannini 1996; Giacintucci et al. 2017, see also Fig. 12). In several cases, the radio emission has a very low surface brightness, which would be extremely difficult to detect observationally, or it is absent altogether.

To compare the performances of different, current, and forthcoming, radio instruments, we present in Fig. 10 X-ray and radio maps of the most massive halo in the TNG300 simulation for different instruments. Radio maps have been computed by assuming model 1 (see Section A2) and for four different instruments, as indicated in the top right-hand corner of each panel, with sensitivity, resolution, and observing frequency given in Table A1. The panels are arranged in such a way that columns display instruments observing at the same frequency, but with increasing resolution moving from top to bottom, and rows instruments with similar spatial resolution.

By looking at the columns it is readily apparent that the increasing resolution level brings out finer details in the radio maps. For the left-hand column, at an observing frequency of 1.4 GHz, VLA and ASKAP have similar sensitivities so the extent of the emitting radio regions remains approximately the same. For the right-hand column, at a much lower frequency of 120 MHz, the superior sensitivity of SKA allows to map radio emission at larger distances. Comparing across rows, i.e. changing the observation

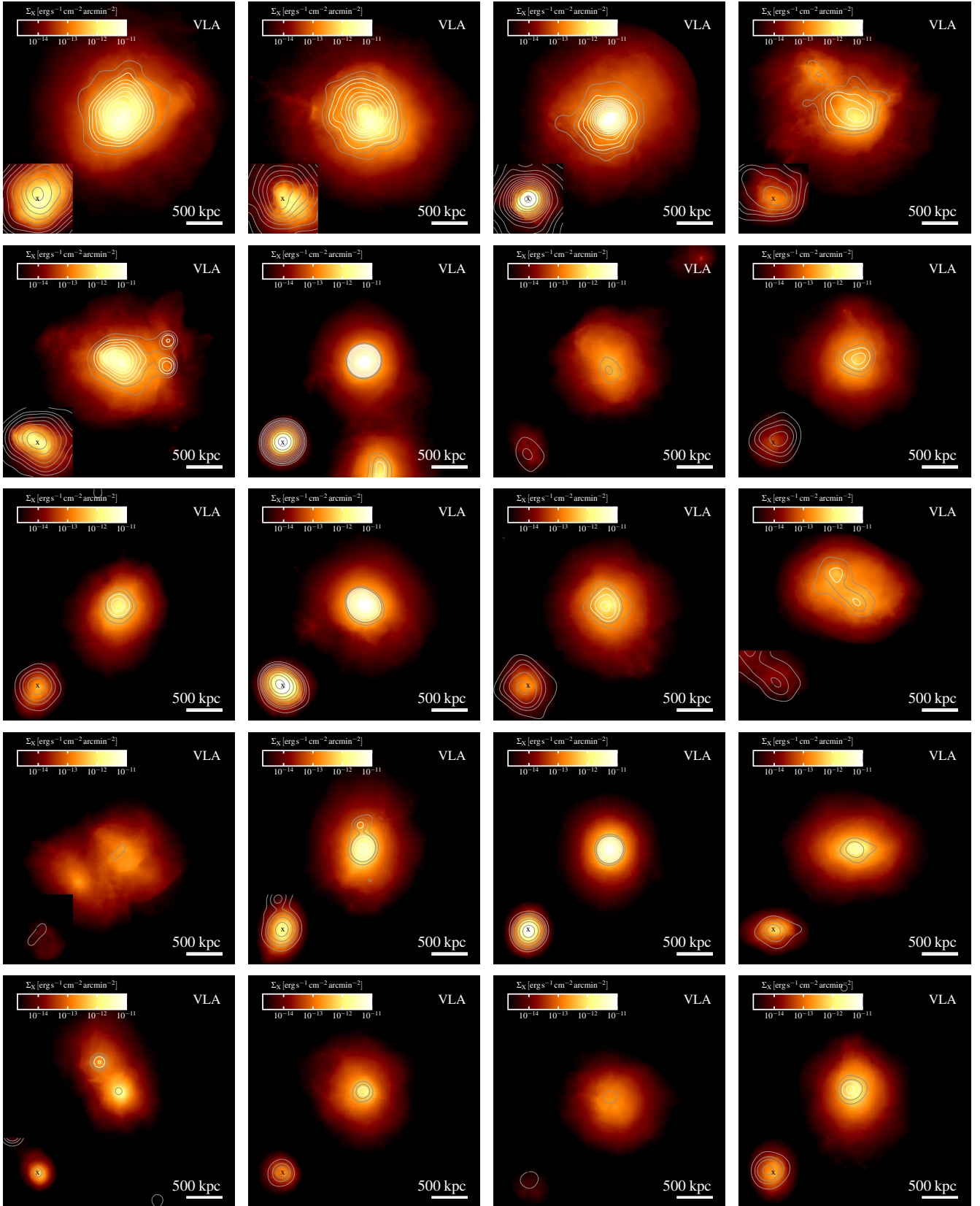


**Figure 9.** As in Fig. 7, but for the 20 most massive haloes of the simulation TNG300. In this case, however, radio maps have been obtained by creating mock VLA observations of radio haloes (see e.g. Govoni et al. 2001; Giovannini et al. 2009; Vacca et al. 2011), with the parameters listed in Table A1. Note that several objects in the sample would not be detected as having extended emission from radio haloes.



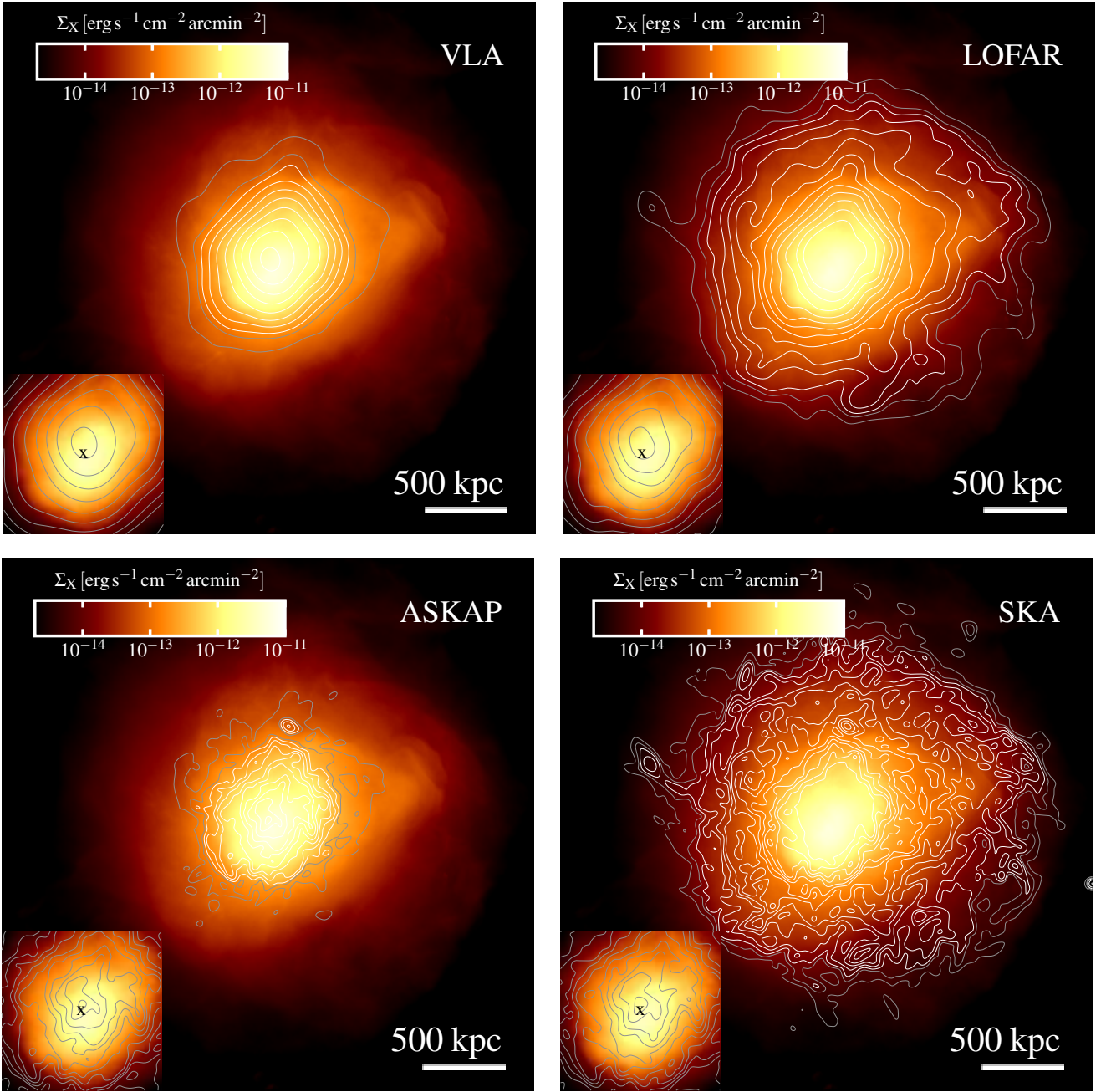


**Figure 10.** X-ray map (colour) overlaid with synchrotron emission contours (computed by assuming model 1 – see Section A2) for the most massive halo of the TNG300 simulation. Each panel is 3.5 Mpc on a side and in projection depth and represents the observation of a different radio telescope. From top left to bottom right these are VLA, LOFAR, ASKAP, and SKA. Contour levels are placed in terms of the noise level at  $1\sigma$  and  $2\sigma$  (grey) and  $3\sigma$  spaced by a  $\sqrt{3}$  factor from one another (white). More details on the radio telescope configurations can be found in Table A1. All maps have been computed for a fiducial redshift of 0.2.

frequency, results in an increase in size of the radio emitting region. Since the telescope sensitivity is similar, the large emitting region is explained by the fact that the emitted radio flux is larger at lower frequency, because of the spectral shape assumed in the map creation. Due to the similar beam size of the instruments, the level of fine details in the radio maps across rows is comparable.

In Fig. 11 we present average radio surface brightness profiles for the 20 most massive haloes of the simulation TNG300 at redshift zero. Profiles are computed in annuli centred on the potential

minimum of each halo with radial bins normalized to the virial radius of each halo. Error bars indicate the  $1\sigma$  dispersion around the mean value. Radio brightness has been computed for the fiducial redshift  $z = 0.2$ . The shaded area indicates values of the radio surface brightness below the  $3\sigma$  rms noise level of each instrument. Simulated emission in this region is considered as non-detected. Red and blue colours in the top left-hand panel present the predictions of radio models 1 and 2, respectively (see Appendix A for details).

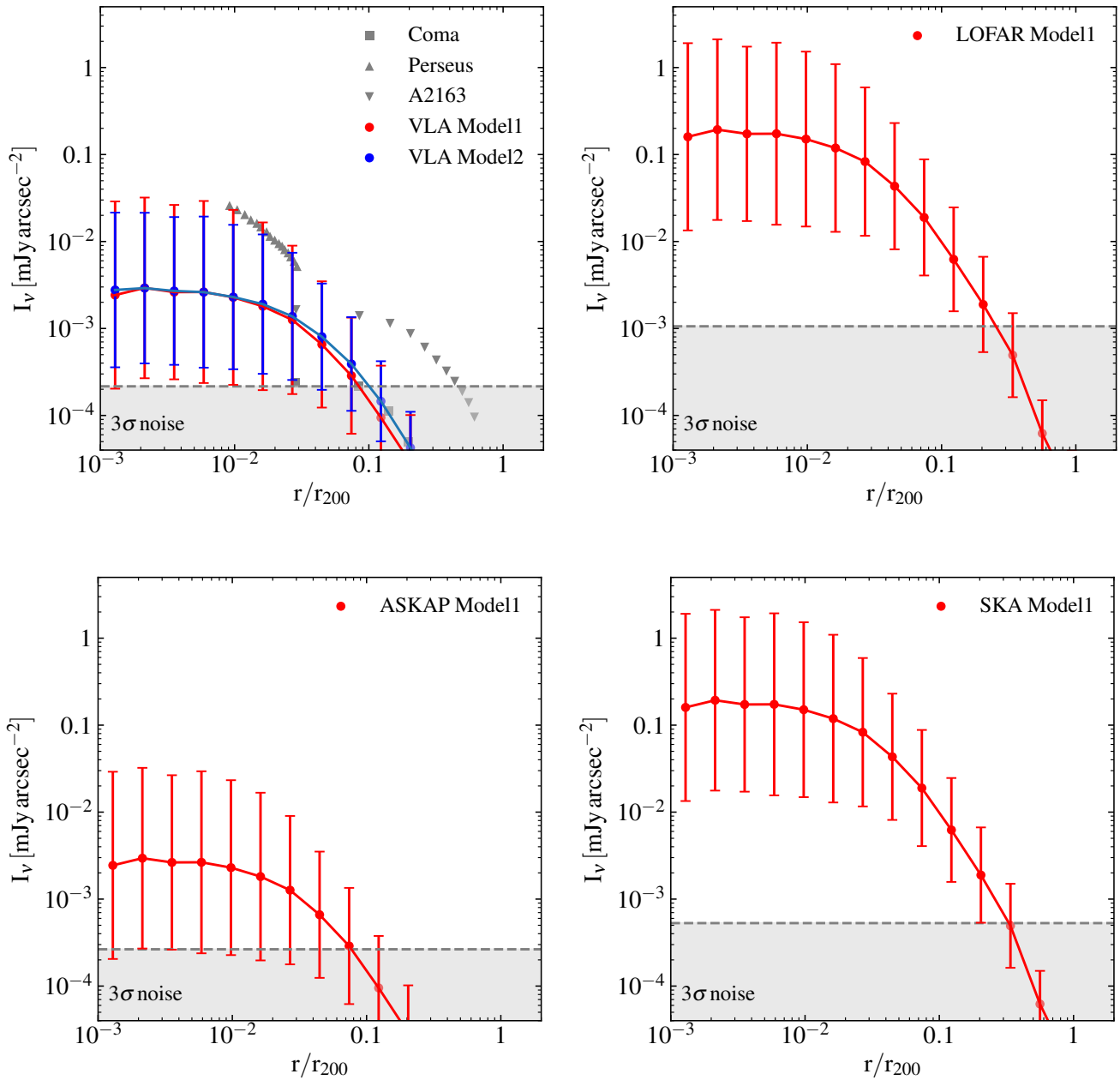


**Figure 11.** Average radio surface brightness profiles for the radio haloes of the 20 most massive haloes in the simulation TNG300 at redshift zero. Synchrotron emission has been averaged in annuli centred on the minimum potential of each halo and results have been binned in radial bins normalized to the virial radius of each object. Error bars indicate the  $1\sigma$  dispersion around the mean value. The synchrotron emissivity has been converted into surface brightness units by assuming a redshift of 0.2 (and determining the luminosity and angular diameter distance given the cosmology) for each source. The shaded area represents the  $3\sigma$  noise level of typical observations of radio haloes in galaxy clusters with the telescopes indicated in the legend (see also Table A1). Emission in the shaded region would not be detected. VLA mock profiles are compared to the actual observed profiles of Coma (Deiss et al. 1997), Perseus (Pedlar et al. 1990), and A2163 (Murgia et al. 2009), as indicated in the legend. Red and blue colours in the top left-hand panel show the predictions of radio model 1 and 2, respectively.

Though there are comparatively large deviations from the mean trend, as shown by the substantial dispersion around the mean values (with model 2 showing generally a smaller scatter, see also the discussion in Section 4.2), the brightness of the synchrotron radiation generally declines with increasing radius. The shape of the decline is roughly exponential. A fit of the mean profiles of

the form  $A \exp(-br/r_{200})$  demonstrates that the cut-off radius of the profiles ( $1/b \approx 0.03-0.05$ ) is approximately the same for all instruments. The central surface brightness depends on the observation frequency. Given the spectral shape of the synchrotron radiation, it is larger for observations at 120 MHz (LOFAR and SKA) by about a factor of 60 compared to instruments observing at 1.4 GHz (VLA



and ASKAP). In the mean profile generated with mock VLA observations, we also report real observed profiles in galaxy clusters (Deiss et al. 1997; Murgia et al. 2009; Pedlar et al. 1990), as indicated in the legend. The values of the simulated profiles are roughly consistent with the observed ones. In particular, the average profile provides a good match to the Coma data, while being marginally consistent with the observed radio profile of Perseus within the relatively large scatter of the simulated data. The discrepancy between the simulated and observed profiles is severe only for the case of A2163, which features a more extended emission than any of the simulated clusters, signalling a general lack of very extended radio haloes in TNG300 (see also Fig. 12). Overall, it can be seen in the observations that radio haloes showing a rather high brightness are more compact than our mean profile. Also, observed objects with lower brightness tend to be more extended than our average brightness profile. No significant differences are found between the findings of radio models 1 and 2.

In Fig. 12, top panel, we present the results of exponential fits of the form  $I_0 \exp(-r/r_e)$  to the surface brightness profiles of the 280 haloes more massive than  $10^{14} M_\odot$  in the simulation TNG300. The profiles to be fit have been generated for the fiducial redshift  $z = 0.2$  and with VLA observing frequency and resolution for synchrotron model 1 (red) and mode 2 (blue), respectively. They extend radially up to a maximum radius of 2 Mpc and they are binned with a spacing given by half the radio FWHM beam size (Murgia et al. 2009). In the plot, we report the values for the best-fitting parameters, together with results obtained from actual observations of radio haloes taken from Murgia et al. (2009). A given halo is present in the plot only if at least three points of the computed radio surface brightness profile are above the instrument sensitivity (calculated as  $3\sigma$ , where sigma is the rms noise level). In this way its brightness profile can be meaningfully fitted with an exponential function. This gives a total of 10 haloes out of the original sample of 280. The grey dashed line separates objects detected as radio haloes (towards large central surface brightness values and characteristic radii) from those that are not detected (lower central brightness values and characteristic radii), but for which it is still possible to perform the surface brightness fit. The line is computed by considering as a detection radio halo profiles for which  $r_{\max} > 2 b_{\text{FWHM}}$ .  $r_{\max}$  is defined as

$$3\sigma = I_0 \exp\left(-\frac{r_{\max}}{r_e}\right), \quad (1)$$

where  $\sigma$  is the instrumental rms noise, while  $2 b_{\text{FWHM}}$  is twice the beam size of the telescope (in this case VLA). This implies the following *minimum* central surface brightness for detection (Murgia et al. 2009)

$$I_0 > 3\sigma \exp\left(\frac{2 b_{\text{FWHM}}}{r_e}\right). \quad (2)$$

Simulated objects detected as extended radio sources according to this criterion are indicated with filled circles, while non-detections are represented by empty circles.

Observationally, galaxy clusters hosting extended radio emission populate two distinct regions. Mini haloes are found at large central brightness values ( $\gtrsim 20 \mu\text{Jy arcsec}^{-2}$ ) and small spatial extent ( $r_e \lesssim 50 \text{ kpc}$ ) while giant radio haloes have relatively low central surface brightness ( $\lesssim 3 \mu\text{Jy arcsec}^{-2}$ ) but a much larger spatial extent ( $r_e$  up to  $\sim 400 \text{ kpc}$ ). While there is roughly the same division in our simulated haloes for radio model 1, radio model 2 features a more continuous distribution with no clear gap at a central surface brightness of  $\gtrsim 10 \mu\text{Jy arcsec}^{-2}$ . Moreover, for both radio

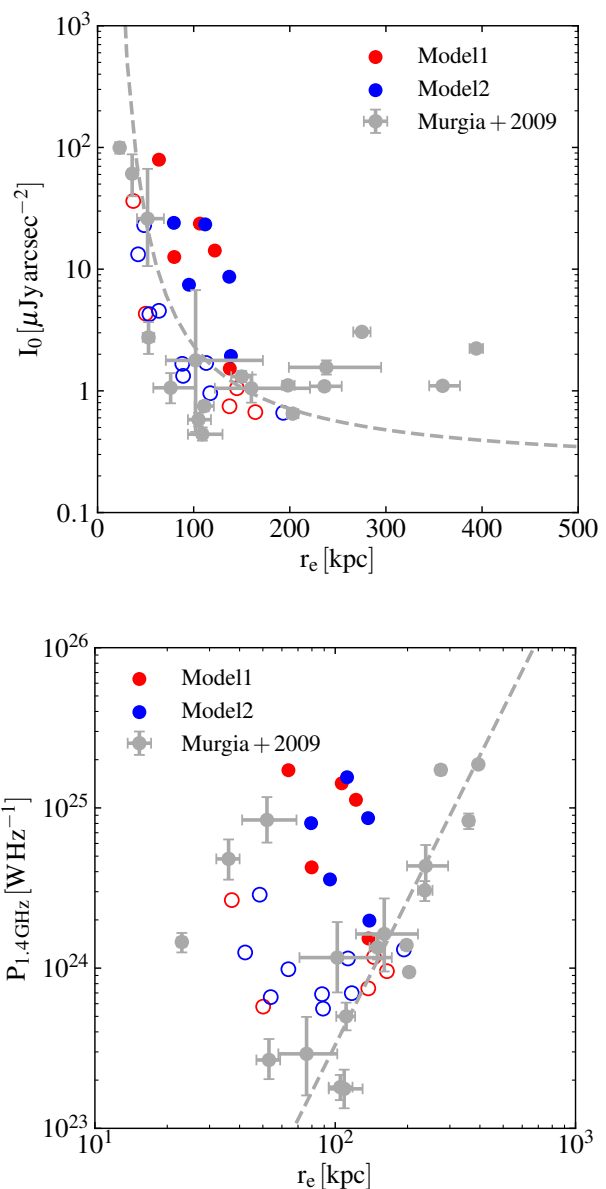


**Figure 12.** Top panel: Exponential fit parameters to the 1.4 GHz radio halo emission of the objects more massive than  $10^{14} M_\odot$  in the TNG300 run. Only objects with at least three detectable points in their mock VLA radio surface brightness have been fitted with a profile of the form  $I(r) = I_0 \exp(-r/r_e)$ . The dashed line shows the threshold for detectability of these sources as extended haloes at a fiducial redshift of 0.2 (see text for details). The simulated objects are divided in detected (filled circles) and non-detected (empty circles) radio haloes according to this criterion. Red and blue colours refer to synchrotron model 1 and model 2, respectively (see Appendix A for details). Observational constraints have been taken from Murgia et al. (2009). Bottom panel: Relation between the radio power at 1.4 GHz and  $r_e$ . The dashed line represents the relation  $\log P_{1.4\text{GHz}} = 23.52 + 3 \log(r_e/100 \text{ kpc})$ , derived for observed giant radio haloes by assuming an average synchrotron emissivity of  $10^{-42} \text{ erg s}^{-1} \text{ cm}^{-2} \text{ Hz}^{-1}$  (Murgia et al. 2009).

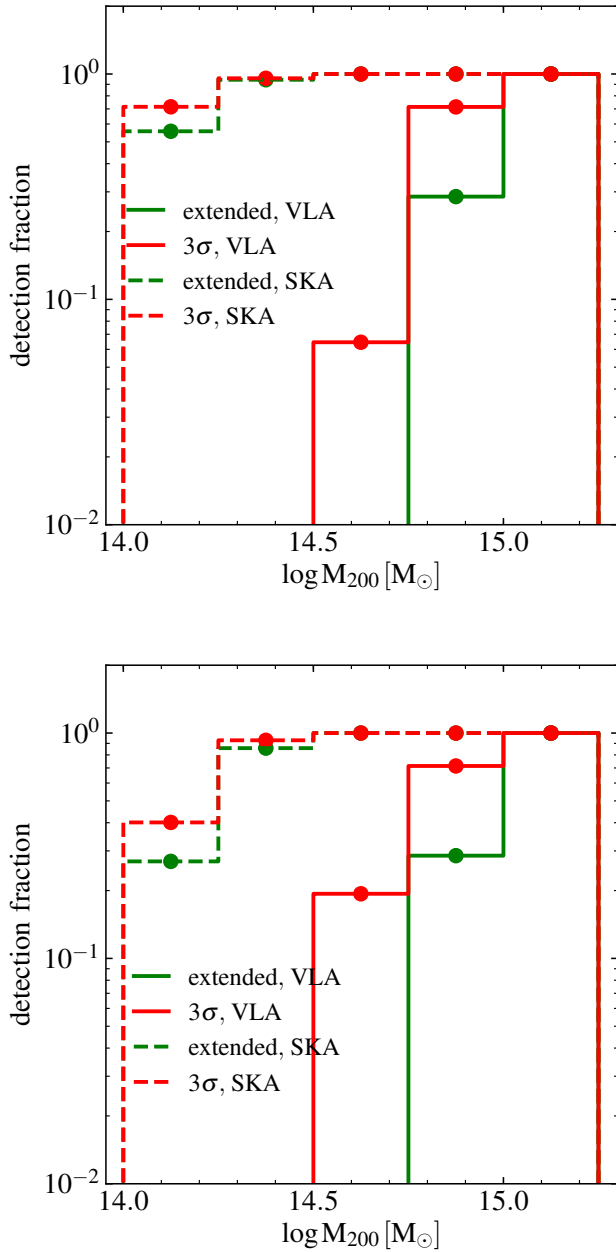


**Figure 13.** Fraction of detected extended radio haloes as a function of virial mass in objects more massive than  $10^{14} M_{\odot}$  for the TNG300 simulation. Solid lines show the detection fraction for mock VLA observations while dashed lines give the corresponding prediction for mock SKA observations. See Table A1 for details on mock observation properties. The different line colours in both panels represent the two different criteria for detection adopted in this work: a central surface brightness cut (Murgia et al. 2009, green) and fixed threshold in surface brightness of three times the rms noise level of the mock observation (red; at least three points must be above the threshold for detection). All mock observations have been created at a fiducial redshift of 0.2. Top and bottom panels show the predictions of synchrotron models 1 and 2, respectively (see Appendix A for details).

models, the group of haloes with high central brightness is in general more extended ( $r_e \sim 100$  kpc) than observed mini haloes. Simulated giant radio haloes match the observed properties quite well. It is apparent that most of the objects hosting giant radio haloes would have a central surface brightness too low for detection with the typical VLA parameters that we have used, and more targeted and sensitive observations would be needed to unveil their radio emission. These more sensitive observations have been performed for all the observed objects present in the figure which are below our adopted detection limit. In general, there appears to be a lack of very extended radio haloes ( $r_e \gtrsim 150$  kpc) in our simulated sample. The giant radio haloes simulated with model 2 appear to be in general more centrally concentrated and less extended than the ones obtained with radio model 1.

The bottom panel of Fig. 12 shows the relation between the radio power at 1.4 GHz and the e-folding radius of the exponential fit of the haloes with a virial mass above  $10^{14} M_{\odot}$  in the TNG300 simulation. This relation is compared to the observational results of Murgia et al. (2009), who find a  $P_{1.4\text{GHz}} \propto r_e^3$  relation for giant radio haloes (the scaling relation that they derive by assuming an average emissivity of  $10^{-42} \text{ erg s}^{-1} \text{ cm}^{-2} \text{ Hz}^{-1}$  for giant radio haloes *only* is shown by the grey dashed line). As in the observations, radio luminosities are computed within  $3 r_e$ . Please note that all the gas cells which are cooling and not star-forming within  $3 r_e$  have been considered and no surface brightness cuts have been imposed. We have estimated the error bars in the radio luminosities of the Murgia et al. (2009) data set by taking the upper and lower bound in the average volumetric synchrotron emissivity and computing the associated luminosities within  $3 r_e$ . This yields luminosity errors that are larger than those presented in Murgia et al. (2009), but this overestimation is not relevant for the analysis carried out in this work. Our simulated results broadly reproduce the division in two groups between giant and mini haloes found observationally for radio model 1. If we divide the sample of our simulated radio haloes in giant haloes and mini haloes by taking a cut in central brightness at  $10 \mu\text{Jy arcsec}^{-2}$  as suggested by a visual inspection of the top panel (giant radio haloes are below this cut whereas mini haloes are above), the simulation predictions match the observational trends for giant radio haloes. With this we mean that their average synchrotron emissivity is comparable with the one ( $\approx 10^{-42} \text{ erg s}^{-1} \text{ cm}^{-2} \text{ Hz}^{-1}$ ) determined observationally. We caution, however, that the majority of the systems would have not been detected for the standard VLA mock observation parameters given in Table A1, and only 1 of 5 objects would have been classified as an extended source according to the criterion presented in equation (2). In the case of mini haloes the agreement is not as good, especially at high luminosities. Specifically, the high luminosity simulated objects are too extended to be part of the mini halo class, but not extended enough to be classified as giant radio haloes. These discrepancies become more pronounced for radio model 2. This is due to the higher central surface brightness and smaller  $r_e$  compared to the values obtained with radio model 1. However, also in this case, the least bright simulated radio haloes have average emissivities in line with those observed in giant radio haloes.

Summarizing, our simulated radio haloes broadly capture the observed dichotomy in surface brightness between mini and giant radio haloes. However, there are noticeable discrepancies with observations, which signal shortcomings of our rather crude modelling for synchrotron emission and might be alleviated by a more sophisticated treatment, for example in the spatial and energy distribution of relativistic electrons.



## 4.2 Observational scaling relations

In Fig. 13 we show the fraction of detected radio haloes as a function of the virial mass of the hosting cluster for the TNG300 simulation. We show this quantity for two radio telescopes observing at different frequencies: VLA (solid lines) and SKA (dashed lines). To estimate the detection fraction we grouped all haloes with virial mass above  $10^{14} M_{\odot}$  in 0.25 dex width mass bins, and computed the fraction of haloes showing detectable radio emission. We used two criteria for detection. The first one, shown with green lines, uses equation (2). The second criterion is less restrictive and considers as detected objects with at least three points in the radial brightness profile above the sensitivity limit ( $3\sigma$  rms noise level, red lines). Radio profiles used to create the figure have been calculated at the fiducial redshift  $z = 0.2$ . Top and bottom panels show the results for synchrotron models 1 and 2, respectively.

Given the comparatively low sensitivity of VLA observations compared to SKA, only haloes with virial masses above  $\sim 3 \times 10^{14} M_{\odot}$  show a significant probability ( $\gtrsim$  a few per cent for model 1 and  $\gtrsim 20$  per cent for model 2) of hosting detectable radio emission. The detection fraction is monotonically increasing with mass, arriving at 100 per cent for the most massive bin. Moreover, there is a difference in the detection fraction trends with respect to the detection criterion adopted. In particular, the less restrictive one, dubbed  $3\sigma$  in the figure caption, yields substantially higher detection fractions at small masses. This discrepancy reduces at the high-mass end, where the trends given by the two criteria come into agreement. For the SKA observations, the increasing trend of the detection fraction with virial mass is also present. Thanks to the superior sensitivity – and also of a larger radio flux at 120 MHz – the detection fractions are substantially larger in this case (above 50 per cent for model 1 and 30 per cent for model 2). The less restrictive detection criterion yields larger detection fractions at small masses. The differences between the two radio models are within a factor of  $\sim 3$ , but are more pronounced at lower virial masses. Interestingly, radio model 2 predicts a fraction of detectable radio haloes that is smaller than radio model 1 in the SKA case, whereas the trend reverses for VLA observations. This is largely due to the fact that the predicted radio luminosities of model 2 in the VLA case are in general somewhat larger at fixed virial mass (see also Fig. 15) than the ones that are obtained in model 1. However, due to the flatter spectral index  $\alpha$  the trend is the opposite at lower frequencies.

In Fig. 14 we show the luminosity function of radio haloes, i.e. source count per comoving unit volume and total radio power, for the TNG300 simulation. All haloes with virial mass above  $10^{14} M_{\odot}$  have been considered. The luminosity function is presented for VLA (top panel) and SKA (bottom panel) mock observations for a fiducial redshift of  $z = 0.2$  and for both radio models 1 (solid lines) and 2 (dashed lines). Both the luminosity function of all the haloes above the adopted mass cut and those of the objects hosting detectable radio emission – according to the criteria presented above – are displayed in the figure. For the VLA case, we have also added observations at 1.4 GHz taken from Zandanel et al. (2014) and based on the NVSS survey (Giovannini et al. 1999). The observed points are derived from an X-ray flux limited sample with 13 detected objects. For the simulated luminosity function, radio luminosities are computed within the virial radius of each object without imposing any cut on surface brightness. The dashed vertical lines present in both panels indicate the luminosity at which the radio luminosity function is complete at the 95 per cent level given our virial mass cut.

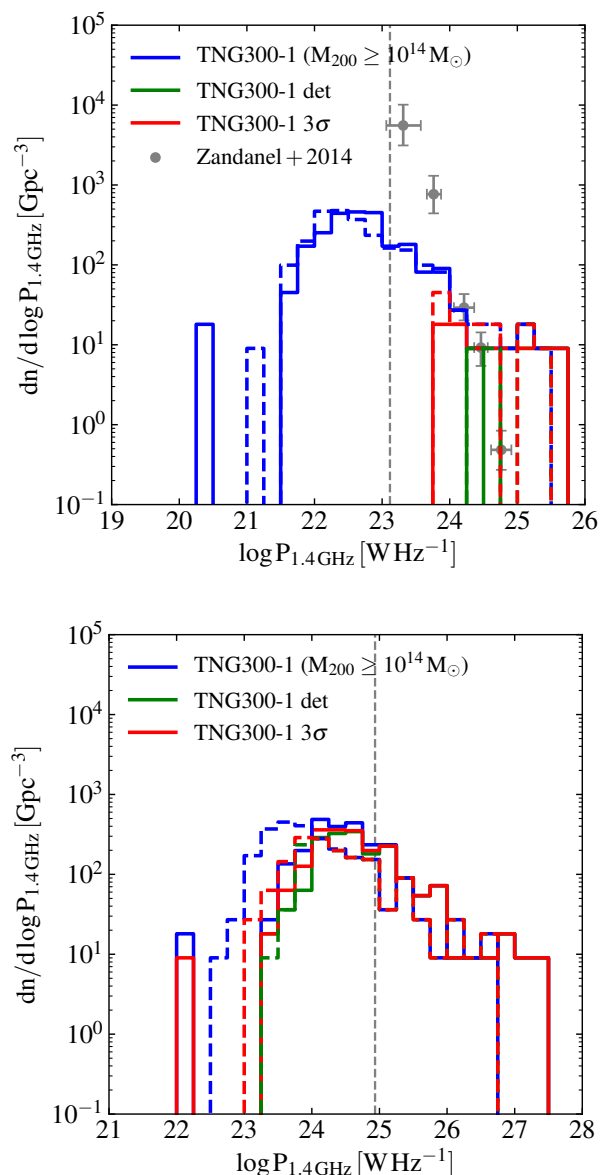


**Figure 14.** Source count per unit volume as a function of the total synchrotron power in the TNG300 simulation for VLA (top) and SKA (bottom) mock observations. Only objects with a virial mass larger than  $10^{14} M_{\odot}$  have been considered. The plots show the resulting source count taking into account all sources above the virial mass cut (blue) or only detectable source according to two different criteria applied to their surface brightness profiles: a central surface brightness cut (Murgia et al. 2009, green) and fixed threshold in surface brightness of three times the rms noise level of the mock observation (red; at least three points must be above the threshold for detection). For both panels a fiducial redshift of 0.2 has been used. Solid and dashed lines show the results for synchrotron models 1 and 2, respectively (more details in Appendix A). The dashed vertical lines indicate a completeness level of 95 per cent given our virial mass cut. VLA mock observations are compared to the NVSS data set obtained in Zandanel et al. (2014, see also Giovannini et al. 1999).

Both panels show the same shape of the luminosity function. At low luminosities the number of radio haloes per unit comoving volume increases with radio power until it reaches a maximum at around  $\sim 10^{22.5} \text{ W Hz}^{-1}$  for VLA and  $\sim 10^{24} \text{ W Hz}^{-1}$  for SKA mock observations. After the peak there is a steady decline of the number of haloes for increasing radio power. Note that this peak is an artefact of the virial mass selection criterion that we have applied to select the cluster sample, which causes the luminosity function to turn over at low luminosities (see also Zandanel et al. 2014). Both luminosity functions cover a span in radio power of about 4 to 5 dex, with SKA mock observations shifted towards higher radio power. The higher radio power for the SKA mock observations is due to the different observing frequency from the VLA in conjunction with the assumed spectral shape for the synchrotron radiation ( $P_\nu \propto \nu^{-\alpha}$ , with  $\alpha = 1.7$  for radio model 1 and  $\alpha = 1.3$  for radio model 2).

When considering only detected haloes, we find some differences. It can be seen that only radio haloes at the most luminous end can be detected. For the VLA case this translates into a minimum power of  $\approx 10^{24} \text{ W Hz}^{-1}$ . The shape of the luminosity function of detected haloes above this minimum power is practically indistinguishable from the total luminosity function, i.e. the red and green lines, which show the luminosity function for detected haloes, cover the blue line, which shows the luminosity function of all the 280 clusters of the sample. There exist small differences in the form of the luminosity function of detected haloes depending on the detection criterion adopted, but in general the agreement is good at high luminosity, in line with the results presented in Fig. 13. Compared to the observations, it can be readily seen that our simulated radio haloes are overly luminous, and the steep drop in the source count is not reproduced by our model. This discrepancy may just be a reflection of our simplified model for relativistic electrons, which are not directly tracked in the simulation. In particular, their energy density follows directly from the magnetic field distribution, and to reproduce the observations a different and more physically motivated distribution of relativistic particles (derived, for instance, as in Zandanel et al. 2014) might be required. For mock SKA observations, the differences in the shape of the luminosity function of detected radio haloes for the two detection criteria that we have adopted in this work is not very pronounced and disappears at high radio power. Differently from the VLA case, the luminosity function of detected haloes extends down to lower luminosities, spanning a larger range in power. This is again due to the superior sensitivity of SKA and the larger synchrotron emission at lower frequencies. The trends of the two different radio models are very similar for VLA mock observation, while there is a shift towards lower radio luminosity for SKA mocks in the case of synchrotron model 2 due to the flatter (1.3 versus 1.7) spectral index adopted.

In Fig. 15, we present the relationship between the total radio power (computed with VLA parameters) within  $r_{500}$  with  $M_{500}$  (top panel) and with Sunyaev-Zel'dovich parameter  $Y_{500}$  (bottom panel) for the haloes more massive than  $10^{14} M_\odot$  in the TNG300 simulation. Observational data (grey squares) are taken from Cassano et al. (2013), whereas red and blue points represent the predictions of radio models 1 and 2, respectively.

There exists a correlation between  $M_{500}$  and radio power, with more massive haloes having larger radio power. The scatter progressively increases towards lower masses in the case of radio model 1, whereas radio model 2 gives rise to a tighter relation across the full mass spectrum. Note that if we had applied the detection criteria discussed previously, only the most massive objects

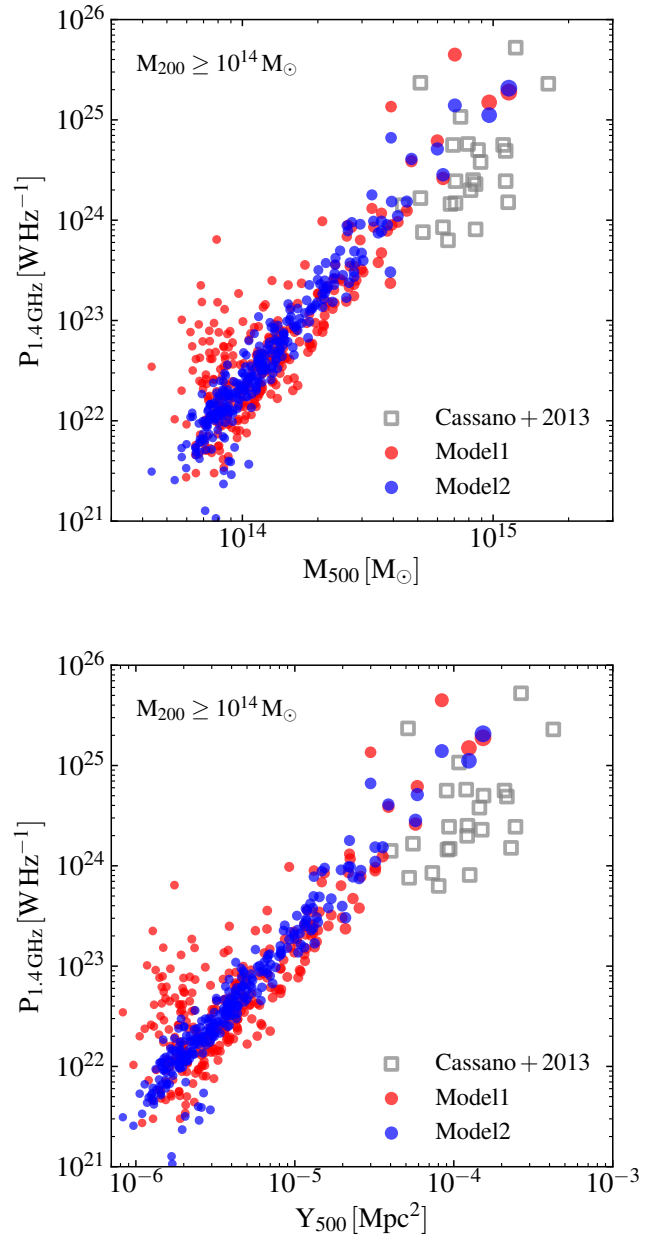


**Figure 15.** Top panel: Total synchrotron power versus  $M_{500}$  for the TNG300 simulation at redshift zero. The radio emissivity has been computed within  $r_{500}$  of each halo and with typical VLA parameters (see Table A1). Only objects with a virial mass larger than  $10^{14} M_\odot$  are shown in this plot. The size of each circle is scaled linearly with the halo virial mass. Bottom panel: Total synchrotron power versus the Sunyaev-Zel'dovich parameter  $Y_{500}$  for the TNG300 simulation at redshift zero. To make this plot the same set up of the top panel has been used. Simulations are compared to data points presented in Cassano et al. (2013). Red points show the predictions for synchrotron model 1, whereas blue points the one obtained for synchrotron model 2 (more details in Appendix A).



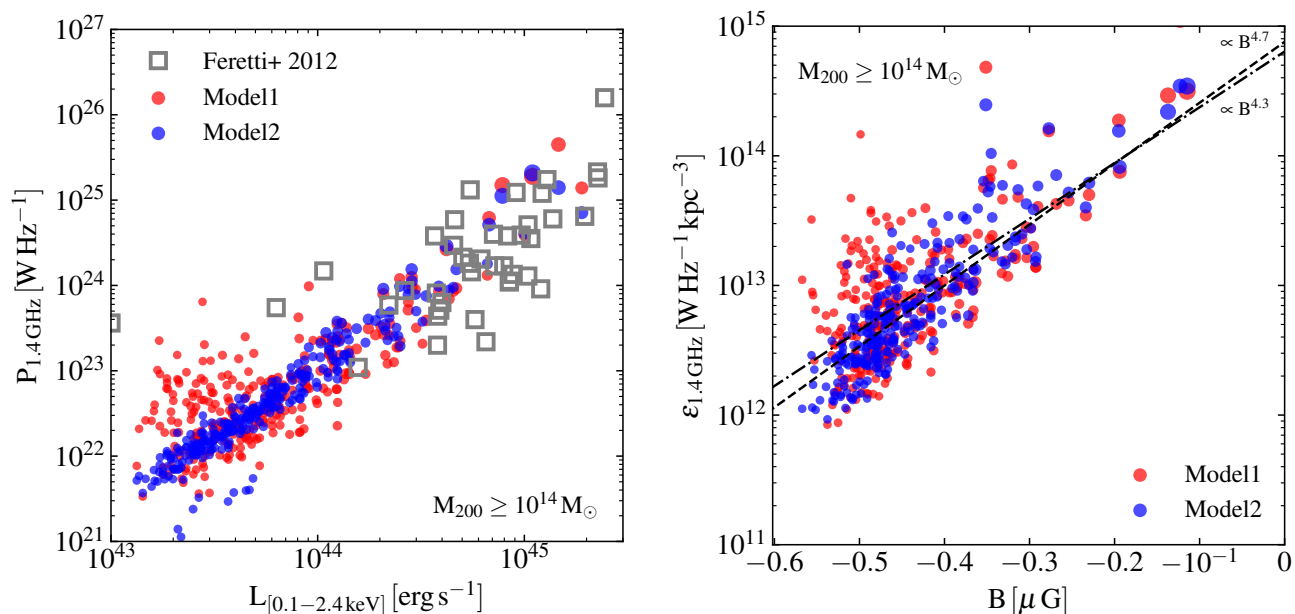


**Figure 16.** Left-hand panel: Total synchrotron power versus X-ray luminosity for the TNG300 simulation at redshift zero. Luminosities for both emission mechanisms have been computed within the virial radius of each halo and only objects with a virial mass larger than  $10^{14} M_{\odot}$  have been considered. The size of each circle is scaled linearly with the halo virial mass. Simulation results are compared with the observed relation for galaxy clusters (grey squares). Data are taken from the list compiled in Table 1 of Feretti et al. (2012, see references therein for studies of individual objects). Right-hand panel: Total synchrotron emissivity versus volume-weighted B field intensity for the TNG300 simulation at redshift zero. The radio emissivity and B field intensity have been computed within the virial radius of each halo and only objects with a virial mass larger than  $10^{14} M_{\odot}$  are shown in this plot. The size of each circle is scaled linearly with the halo virial mass. The black dashed lines show the expected scaling of the radio emissivity ( $\epsilon \propto B^{3+\alpha}$ ) for the synchrotron emission models used in this work ( $\alpha = 1.7$  for model 1 and  $\alpha = 1.3$  for model 2, respectively). Radio power and emissivities have been computed with typical VLA parameters (see Table A1). In both panels red points show the relations for synchrotron model 1, whereas blue points the one obtained for synchrotron model 2 (see Appendix A).

$M_{200} \gtrsim 10^{14.5} M_{\odot}$  in this plot would have been detected (see Fig. 13 on the detection probability). Compared to the observations, the scaling relations examined here at the high-mass end is tighter and less steep. Moreover, there is no clear indication of the observed bimodal behaviour in the radio emission – only about 30 per cent of the observed massive/luminous clusters possess detectable radio emission – for clusters at high masses (or equivalently high X-ray luminosity, e.g. Brunetti et al. 2007). The tightness of the relationship, and the absence of bi-modality, are a consequence of the assumption that the energy density of relativistic electrons is proportional to the energy content of the B field in each cell. This occurs also for radio model 2, although in this case the relativistic electron energy density is normalized to the cluster thermal energy content. However, the ratio between magnetic and thermal energies in our simulated cluster is approximately constant at about 1% level (see Fig. 6, bottom right-hand panel).

The steepness of the relation can be varied by changing the assumed spectral index  $\alpha$  of the synchrotron radiation, which determines the dependence of the radiated radio power on the B field strength in our model (see Appendix A). However, we caution that changing  $\alpha$  has also an effect on the normalization of this scaling relation other than on its slope, and that there exist different, but still physically motivated, parametrizations controlling synchrotron emissivity in our model that can reproduce the observations equally well, as it is explicitly demonstrated by the choices of parameters adopted in our radio models 1 and 2. There is no obvious way, with our present models for synchrotron-emitting electrons, to increase the scatter of the correlation at high virial masses nor to reproduce

the observed bimodality in the population of radio emitting clusters (e.g. Kale et al. 2015), which therefore still remains an unsolved issue in our simulations. Finally, we would also like to mention that in our current modelling there is no evidence of a dependence of radio emission with the host halo dynamical state (e.g. Cassano et al. 2010). These shortcomings call for a more sophisticated treatment of relativistic particles in our analysis.

The same considerations also apply to the  $P_{1.4\text{GHz}}$  versus  $Y_{500}$  relation. We would like to note that the same set of parameters controlling the radio emissivity can reproduce both scaling relations with a comparable level of accuracy. This is expected, since the  $Y_{500}$  Compton parameter is also used in observations to estimate total cluster masses, being proportional to the gas mass enclosed within  $r_{500}$  and therefore to  $M_{500}$  (see e.g. Cassano et al. 2013, equation 2). This is another indirect confirmation that our galaxy cluster sample features realistic gas fractions, therefore addressing one of the major Illustris issues (Genel et al. 2014). Cluster gas fractions and scaling relations will be analysed in more detail in future work.

In Fig. 16, we present scaling relations for galaxy clusters, relating magnetic fields, radio emission properties and cluster X-ray emission for all haloes more massive than  $10^{14} M_{\odot}$  in the TNG300 simulation. The figure relates the total radio power at 1.4 GHz to the total X-ray luminosity in the [0.1 – 2.4] keV energy band (left-hand panel), and the synchrotron emissivity at 1.4 GHz as a function of the volume-weighted average magnetic field strength within the virial radius of each object (right-hand panel). Each panel presents the results for both radio model 1 (red symbols) and 2 (blue symbols). For the left-hand panel, we compare our result to observa-

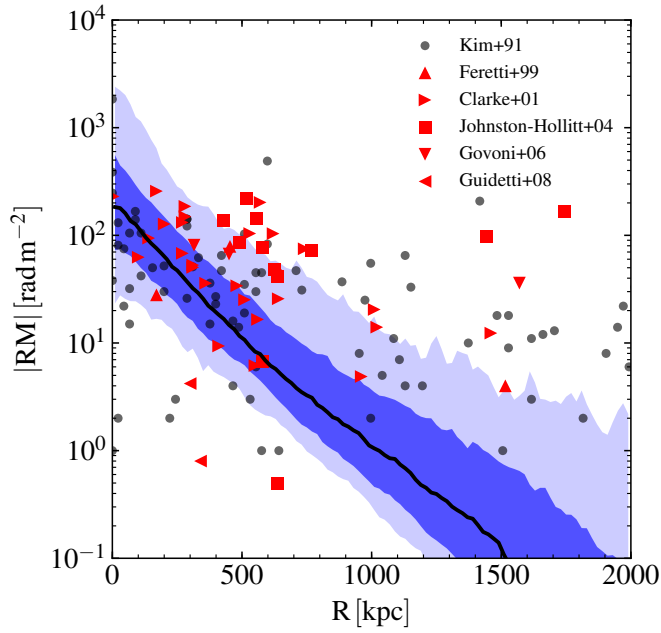


**Figure 17.** Radial profile of the absolute value of the Faraday rotation measure for haloes with  $M_{200} > 10^{14} M_{\odot}$  in the TNG300 simulation. The solid black line represents the median profile of the sample while the dark blue and the light blue regions enclose the 16th – 84th and the 2nd – 98th percentiles, respectively. Simulation results are compared to actual measurements of rotation measure in galaxy clusters (coloured symbols) taken from the references indicated in the legend.

tional findings collected in [Feretti et al. \(2012\)](#). We use this comparison to calibrate the free parameters of our radio emission models in such a way that it broadly matches this scaling relation at the high-mass end, where radio emission is detected for galaxy clusters. The parameters that we have chosen are compatible with theoretical and observational estimates (see Appendix A for their values). The interpretation of these results largely follows the discussion already presented for Fig. 15, given the relation between the cluster  $M_{500}$  and its X-ray emission. For the right-hand panel, we compare the results to the expected scaling for the synchrotron emissivity of our models (dashed and dash-dotted black lines), which are proportional to  $B^{4.7}$  and  $B^{4.3}$ , for models 1 and 2, respectively<sup>3</sup> (see again Appendix A). At low average magnetic fields, which in general correspond to low virial masses, the emissivity values present a large scatter (more pronounced in the case of radio model 1), while the relation progressively tightens at larger average magnetic field intensities (large virial masses). The expected scaling is reproduced quite well, but globally the relation appears to be slightly steeper than the theoretical expectation. However, it is difficult to establish a trend given the significant dispersion in the radio emissivity at low virial masses.

In Fig. 17 we present the median radial profile of the Faraday rotation measure (RM) for all haloes with  $M_{200} > 10^{14} M_{\odot}$  in the

TNG300 simulation. RM is defined as

$$RM = \frac{e^3}{2\pi m_e^2 c^4} \int_0^L n_e(s) B_{\parallel}(s) ds, \quad (3)$$

where  $e$ ,  $m_e$ , and  $c$  are the electron charge, electron mass, and speed of light, respectively;  $n_e$  is the electron density and  $B_{\parallel}$  is the component of the magnetic field along the line-of-sight element  $ds$ , and gives information about the strength and coherence length of the magnetic field, being therefore dependent on its amplification and topology. We compute the RM using a similar set up as for the X-ray and radio maps of Fig. 9. For each pixel of the map – which extends two times the virial radius of each object across and uses a pixel size of 2 kpc – equation (3) is computed. Then pixels are radially binned in 100 equally spaced bins in the radial range 0 – 2000 kpc and the RM profile for each halo is extracted. The median (solid black line) and the associated percentiles of the distribution showing the spread of the values (dark and light blue, see caption for details) are finally determined and plotted. Simulation results are compared to actual measurement of RM in galaxy clusters (coloured symbols) taken from [Kim et al. \(1991\)](#); [Feretti et al. \(1999\)](#); [Clarke et al. \(2001\)](#); [Johnston-Hollitt & Ekers \(2004\)](#); [Govoni et al. \(2006\)](#); [Guidetti et al. \(2008\)](#), as indicated in the legend.

It can be seen that the median RM profile is a declining function of the radius. Overall there is a good agreement between the RM values of the simulated clusters and the observations especially in the innermost regions ( $R \lesssim 1000$  kpc). At larger distances our median profile is declining too fast compared to the observations (see also [Marinacci et al. 2015](#)). This faster decline is likely due to insufficient resolution at large distances. This in turn is caused by the pseudo-Lagrangian nature of the default refinement scheme adopted in AREPO, which tries to keep the gas cell mass within a factor of two from a predefined target mass, effectively making spatial resolution dependent on gas density ([Nelson et al. 2016](#)). However, higher resolution simulations targeted at individual galaxy clusters (see e.g. [Vazza et al. 2018](#)) are needed to fully investigate this aspect. There is a large spread in the values of the RM in both panels, which is becoming more pronounced at larger distances. The large spread is a consequence of either (i) the turbulent amplification of the B field within haloes, (ii) an indication of general lack of resolution, or (iii) missing physics within our model that can reorient the magnetic field (e.g. thermal conduction, [Kannan et al. 2016a](#)). We also note that the computation of the RM signal is sensitive to the pixel size used to produce the map. Therefore the results can also depend on this choice, although increasing or decreasing the pixel size by a factor of a few (up to 10 kpc) does not lead to a dramatic change of the median RM profile.

Finally, we would like to point out that in our analysis we did not attempt to distinguish between different types of galaxy clusters. This is of course a simplification because some of the scaling relations that we have investigated (e.g. rotation measure profiles and the relation between radio and X-ray luminosities) have been determined for objects falling into disjoint classes (e.g. relaxed clusters with a cool core and merging clusters). The fact that we are able to reproduce to some extent these observational relations in our cluster sample stems from the observation that our simulated clusters show a continuum of properties that at the extreme ends encompass cool-core and non-cool core systems (with no strong dichotomy present unlike suggested by observations, see [Barnes et al. 2018](#)) combined with the large scatter in the relations that we have investigated, in particular in the values of the rotation measure.

<sup>3</sup> The scaling for model 2 implicitly assumes that the ratio between magnetic and thermal energy densities within each cluster is constant. This appears to be a good approximation in our simulated clusters (see Fig. 6, bottom right-hand panel).

## 5 SUMMARY AND CONCLUSIONS

We have introduced the IllustrisTNG project, the successor of Illustris, and presented the general properties of radio haloes and magnetic fields in the TNG100 and TNG300 simulations, which are the most novel physics aspects of IllustrisTNG compared to Illustris.

We first quantified the magnetic field strengths as a function of environment, and then specifically explored the scaling relations between the total radio power and various cluster properties (mass, X-ray emission, and SZ signal), the structural properties of radio haloes (central surface brightness, spatial extent, and radial profiles), and the detection fraction and luminosity function of such objects. We have performed a detailed comparison to current and upcoming observational data by producing mock radio observations for VLA, LOFAR, ASKAP, and SKA. Our cluster sample represents the largest numerically studied radio halo sample to date including 280 haloes above a virial mass of  $10^{14} M_{\odot}$ . Our main results can be summarized as follows:

- The magnetic field intensity traces density peaks in the matter distribution closely. At low overdensities (i.e. in filaments and voids,  $\rho/\langle\rho_b\rangle \lesssim 10^2$ ), the intensity of magnetic fields scales according to flux conservation ( $B \propto \rho^{2/3}$ ). Closer to and within haloes ( $\rho/\langle\rho_b\rangle \gtrsim 10^2$ ) additional processes, such as gas turbulent motions and shear flows, amplify magnetic fields up to  $\sim 10 \mu\text{G}$ , a value that is 4 to 5 orders of magnitude larger than the value expected from ‘flux freezing’. By  $z = 2$ , most of the magnetic field amplification at large overdensities has already occurred. We do not find large differences in these trends in the two simulation boxes (TNG100 and TNG300) analysed in this work. Only in the transition region between low-density and high-density gas ( $\rho/\langle\rho_b\rangle \sim 10^2$ ) and at high redshift ( $z = 2$ ), the magnetic field amplification in the TNG300 simulation is less pronounced than in TNG100 because of the lower resolution of the former run.

- The magnetic field topology within galaxies depends on their morphology and in particular on the existence of a rotationally supported gaseous disc. In early-type galaxies, in which a gaseous disc is largely absent due to the disruptive effects of the AGN feedback, the field orientation is not well defined although magnetic fields tend to align with gas filaments if any is present. Disc galaxies generally feature an ordered, large-scale magnetic field in the disc plane, which is also (anti-)aligned with the gas velocity field.

- Within haloes, magnetic field intensities are declining with radius. The field strength tends to decline faster once a radial distance of  $\sim 0.3 r_{200}$  is reached. In the halo centres the field intensity reaches values of  $\sim 10 \mu\text{G}$ , in line with observational determinations, to then drop by about three orders of magnitude in the external regions. This value is however larger than the one expected from ‘flux freezing’, signalling again the efficient magnetic field amplification occurring within haloes. There is good agreement between the results obtained from TNG100 and TNG300 notwithstanding the coarser resolution of the latter.

- The ratio between magnetic and thermal pressure  $\beta^{-1}$  reaches maximum values of about 3 in halo centres ( $r \sim 0.1 r_{200}$ ) for virial masses  $\lesssim 10^{12.5} M_{\odot}$ . This value declines with virial mass and for increasing distances from the halo centres. In the most massive haloes ( $M_{200} \gtrsim 10^{13.5} M_{\odot}$ )  $\beta^{-1} \approx 10^{-2}$ , and this value remains basically constant with radius. In general, magnetic fields are dynamically unimportant on the scales resolved in IllustrisTNG. Again, the agreement between the results obtained from TNG100 and TNG300 is very good.

- Our simulated galaxy clusters show extended radio emission with morphology that matches the extension and shape of bremsstrahlung X-ray radiation originating from the hot gas. The detectability of this radio emission depends on the mass of the cluster – more X-ray luminous/massive clusters are easier to detect in radio – and on the sensitivity and the observing frequency of the radio telescope. In particular, we find that in current radio surveys (VLA mock observations) only clusters with a virial mass larger than  $\sim 3 \times 10^{14} M_{\odot}$  have a significant probability ( $\gtrsim$  few per cent) of hosting detectable radio emission, which increases steadily reaching 100 per cent for the most massive ( $M_{200} \sim 10^{15} M_{\odot}$ ) objects. The minimum virial mass for detection decreases down to  $10^{14} M_{\odot}$  (the lowest virial mass analysed in this paper) for SKA mock observations. Moreover, the detection probability for SKA mock observations is substantially larger – above 30 per cent at all masses – and shows the same increasing trend with virial mass.

- Emission from radio haloes exhibits a radially declining profile, which is described quite well by an exponential. At the fiducial redshift  $z = 0.2$  used to generate the mock radio maps, central surface brightnesses, averaged over the 20 most massive objects of our simulated sample, of  $\approx 3 \times 10^{-3} \text{ mJy beam}^{-1}$  for instruments observing at 1.4 GHz (such as VLA and ASKAP) or of  $\approx 0.2 \text{ mJy beam}^{-1}$  for instruments observing at a 140 MHz (such as LOFAR and SKA) are reached, respectively. On average, radio emission is detectable up to  $0.1 - 0.3 r_{200}$  after which it goes below the  $3\sigma$  instrument sensitivity. The simulated VLA profiles are broadly consistent with observations although discrepancies from the observed trends are noticeable. In particular, observed clusters featuring high radio surface brightness are more compact than the simulated objects, while observed radio haloes with lower surface brightness appear to be more radially extended than our findings.

- The average trends are in agreement with the results of fitting exponential surface brightness profiles to our simulated radio haloes on an object by object basis. The fitting procedure reveals that, while our simulations broadly capture the observational division between mini and giant radio haloes, the simulated mini haloes are in general more extended ( $r_e \sim 100 \text{ kpc}$ ) than their observed counterpart ( $r_e \sim 50 \text{ kpc}$ ) and there is a general lack of very extended ( $r_e \gtrsim 150 \text{ kpc}$ ) radio haloes in our simulated sample. The relationship between the total radio luminosity with  $r_e$  ( $P_{1.4 \text{ GHz}} \propto r_e^3$ ) is roughly recovered in our simulations for giant haloes for radio model 1 and the least bright haloes of model 2, while our simulated mini haloes appear to be too extended for their radio luminosity.

- We find a good agreement with scaling relations observed between the total radio power and galaxy cluster properties – such as mass, X-ray luminosity, SZ Compton parameter. Calibrating the free parameters of our radio emission modelling on one of these relations (we have adopted the radio power versus X-ray luminosity relation in this work) reproduces the other scaling relations with the same degree of accuracy. This presents further evidence that the magnetic field amplification (which controls the total radio power in our model) and the assembly of the cluster and its ICM are tightly linked.

Our results indicate that the magnetic field properties predicted by our simulations are in line with various observational constraints. There are, however, some tensions. Those are inevitable due to the rather simple models that we have adopted to describe relativistic particles, whose evolution is not followed self-consistently in the IllustrisTNG simulations. These shortcomings



of our treatment of relativistic particles can likely be addressed with a more complete description of their spatial and energy distributions (e.g. [Pinzke et al. 2017](#)), or by directly modelling their evolution in a self-consistent way in the simulations ([Pfrommer et al. 2017](#)). We intend to explore both possibilities, and thus present a more detailed characterization of radio emission in simulated galaxy clusters, in future work adopting a galaxy formation model going beyond this limitation of IllustrisTNG.

## ACKNOWLEDGEMENTS

We thank an anonymous referee for insightful comments that helped improving the paper. FM also thanks Christoph Pfrommer, Irina Zhuravleva, and Rahul Kannan for helpful discussions on radio haloes in galaxy clusters. VS, RW, and RP acknowledge support through the European Research Council under the ERC-StG grant EXAGAL-308037 and would like to thank the Klaus Tschira Foundation. MV acknowledges support through an MIT RSC award, the support of the Alfred P. Sloan Foundation, and by the NASA ATP grant NNX17AG29G. SG and PT are supported by NASA through Hubble Fellowship grants HST-HF2-51341.001-A and HST-HF2-51384.001-A, respectively, awarded by the STScI, which is operated by the Association of Universities for Research in Astronomy, Inc., for NASA, under contract NAS5-26555. JN acknowledges the support of the NSF AARF award AST-1402480. The Flatiron Institute is supported by the Simons Foundation. Simulations were run on the Hazel-Hen Cray XC40-system at the High Performance Computing Centre Stuttgart as part of project GCS-ILLU of the Gauss Centre for Supercomputing (GCS). Additional simulations were carried out on the Hydra and Draco supercomputers at the Max Planck Computing and Data Facility, on the Stampede supercomputer at the Texas Advanced Computing Center through the XSEDE project AST140063, and on the joint MIT-Harvard computing cluster supported by MKI and FAS. All the figures in this work were produced by using the MATPLOTLIB graphics environment ([Hunter 2007](#)).

## REFERENCES

- Ackermann M., et al., 2016, *ApJ*, **819**, 149
- Anderson M. E., Bregman J. N., 2010, *ApJ*, **714**, 320
- Arlen T., et al., 2012, *ApJ*, **757**, 123
- Barnes D. J., et al., 2018, *MNRAS*, in press,
- Basu A., Roy S., 2013, *MNRAS*, **433**, 1675
- Beck R., 2009, *Astrophysics and Space Sciences Transactions*, **5**, 43
- Beck R., 2015, *A&ARv*, **24**, 4
- Beck R., Wielebinski R., 2013, *Magnetic Fields in Galaxies*. p. 641, doi:10.1007/978-94-007-5612-0\_13
- Beck R., Brandenburg A., Moss D., Shukurov A., Sokoloff D., 1996, *ARA&A*, **34**, 155
- Blasi P., Colafrancesco S., 1999, *Astroparticle Physics*, **12**, 169
- Bonafede A., Feretti L., Murgia M., Govoni F., Giovannini G., Dallacasa D., Dolag K., Taylor G. B., 2010, *A&A*, **513**, A30
- Bravi L., Gitti M., Brunetti G., 2016, *MNRAS*, **455**, L41
- Brunetti G., Venturi T., Dallacasa D., Cassano R., Dolag K., Giacintucci S., Setti G., 2007, *ApJ*, **670**, L5
- Brunetti G., Cassano R., Dolag K., Setti G., 2009, *A&A*, **507**, 661
- Brunetti G., Zimmer S., Zandanel F., 2017, *MNRAS*, **472**, 1506
- Cassano R., Gitti M., Brunetti G., 2008, *A&A*, **486**, L31
- Cassano R., Etori S., Giacintucci S., Brunetti G., Markevitch M., Venturi T., Gitti M., 2010, *ApJ*, **721**, L82
- Cassano R., et al., 2013, *ApJ*, **777**, 141
- Cassano R., et al., 2015, *Advancing Astrophysics with the Square Kilometre Array (AASKA14)*, p. 73
- Cho J., Ryu D., 2009, *ApJ*, **705**, L90
- Clarke T. E., Kronberg P. P., Böhringer H., 2001, *ApJ*, **547**, L111
- Condon J. J., Cotton W. D., Greisen E. W., Yin Q. F., Perley R. A., Taylor G. B., Broderick J. J., 1998, *AJ*, **115**, 1693
- Deiss B. M., Reich W., Lesch H., Wielebinski R., 1997, *A&A*, **321**, 55
- Dolag K., Enßlin T. A., 2000, *A&A*, **362**, 151
- Dolag K., Bartelmann M., Lesch H., 1999, *A&A*, **348**, 351
- Dolag K., Bartelmann M., Lesch H., 2002, *A&A*, **387**, 383
- Dolag K., Grasso D., Springel V., Tkachev I., 2005, *J. Cosmol. Astropart. Phys.*, **1**, 009
- Dolag K., Komatsu E., Sunyaev R., 2016, *MNRAS*, **463**, 1797
- Donnert J., Dolag K., Brunetti G., Cassano R., 2013, *MNRAS*, **429**, 3564
- Enßlin T., Pfrommer C., Miniati F., Subramanian K., 2011, *A&A*, **527**, A99
- Evans C. R., Hawley J. F., 1988, *ApJ*, **332**, 659
- Feretti L., Giovannini G., 1996, in *Ekers R. D., Fanti C., Padrielli L., eds, IAU Symposium Vol. 175, Extragalactic Radio Sources*. p. 333
- Feretti L., Dallacasa D., Govoni F., Giovannini G., Taylor G. B., Klein U., 1999, *A&A*, **344**, 472
- Feretti L., Bonafede A., Giovannini G., Govoni F., Murgia M., 2010, *Highlights of Astronomy*, **15**, 459
- Feretti L., Giovannini G., Govoni F., Murgia M., 2012, *A&ARv*, **20**, 54
- Gaspari M., Brighenti F., Temi P., 2012, *MNRAS*, **424**, 190
- Genel S., et al., 2014, *MNRAS*, **445**, 175
- Giacintucci S., 2011, *Mem. Soc. Astron. Italiana*, **82**, 541
- Giacintucci S., Markevitch M., Cassano R., Venturi T., Clarke T. E., Brunetti G., 2017, *ApJ*, **841**, 71
- Giovannini G., Feretti L., Venturi T., Kim K.-T., Kronberg P. P., 1993, *ApJ*, **406**, 399
- Giovannini G., Tordi M., Feretti L., 1999, *New Astron.*, **4**, 141
- Giovannini G., Bonafede A., Feretti L., Govoni F., Murgia M., Ferrari F., Monti G., 2009, *A&A*, **507**, 1257
- Govoni F., Feretti L., Giovannini G., Böhringer H., Reiprich T. H., Murgia M., 2001, *A&A*, **376**, 803
- Govoni F., Murgia M., Feretti L., Giovannini G., Dolag K., Taylor G. B., 2006, *A&A*, **460**, 425
- Govoni F., Ferrari C., Feretti L., Vacca V., Murgia M., Giovannini G., Perley R., Benoist C., 2012, *A&A*, **545**, A74
- Guidetti D., Murgia M., Govoni F., Parma P., Gregorini L., de Ruiter H. R., Cameron R. A., Fanti R., 2008, *A&A*, **483**, 699
- Hahn O., Abel T., 2011, *MNRAS*, **415**, 2101
- Hunter J. D., 2007, *Computing In Science & Engineering*, **9**, 90
- Johnston-Hollitt M., Ekers R. D., 2004, preprint, (arXiv:astro-ph/0411045)
- Jones T. W., Porter D. H., Ryu D., Cho J., 2011, preprint, (arXiv:1108.1369)
- Kale R., et al., 2015, *A&A*, **579**, A92
- Kannan R., Springel V., Pakmor R., Marinacci F., Vogelsberger M., 2016a, *MNRAS*, **458**, 410
- Kannan R., Vogelsberger M., Stinson G. S., Hennawi J. F., Marinacci F., Springel V., Macciò A. V., 2016b, *MNRAS*, **458**, 2516
- Kim K.-T., Tribble P. C., Kronberg P. P., 1991, *ApJ*, **379**, 80
- Longair M. S., 2011, *High Energy Astrophysics*. Cambridge University Press, Cambridge, UK
- Marinacci F., Vogelsberger M., 2016, *MNRAS*, **456**, L69
- Marinacci F., Vogelsberger M., Mocz P., Pakmor R., 2015, *MNRAS*, **453**, 3999
- Murgia M., Govoni F., Feretti L., Giovannini G., Dallacasa D., Fanti R., Taylor G. B., Dolag K., 2004, *A&A*, **424**, 429
- Murgia M., Govoni F., Markevitch M., Feretti L., Giovannini G., Taylor G. B., Carretti E., 2009, *A&A*, **499**, 679
- Naiman J. P., et al., 2018, *MNRAS*,
- Nelson D., et al., 2015, *Astronomy and Computing*, **13**, 12
- Nelson D., Genel S., Pillepich A., Vogelsberger M., Springel V., Hernquist L., 2016, *MNRAS*, **460**, 2881
- Nelson D., et al., 2018, *MNRAS*, **475**, 624
- Norris R. P., et al., 2013, *Publ. Astron. Soc. Australia*, **30**, e020

- Pakmor R., Springel V., 2013, *MNRAS*, **432**, 176
- Pakmor R., Bauer A., Springel V., 2011, *MNRAS*, **418**, 1392
- Pakmor R., Marinacci F., Springel V., 2014, *ApJ*, **783**, L20
- Pakmor R., Pfrommer C., Simpson C. M., Kannan R., Springel V., 2016, *MNRAS*, **462**, 2603
- Pakmor R., et al., 2017, *MNRAS*, **469**, 3185
- Pedlar A., Ghataure H. S., Davies R. D., Harrison B. A., Perley R., Crane P. C., Unger S. W., 1990, *MNRAS*, **246**, 477
- Persic M., Rephaeli Y., 2014, *A&A*, **567**, A101
- Pfrommer C., Enßlin T. A., Springel V., 2008, *MNRAS*, **385**, 1211
- Pfrommer C., Pakmor R., Schaal K., Simpson C. M., Springel V., 2017, *MNRAS*, **465**, 4500
- Pillepich A., et al., 2018a, *MNRAS*, **473**, 4077
- Pillepich A., et al., 2018b, *MNRAS*, **475**, 648
- Pinzke A., Pfrommer C., 2010, *MNRAS*, **409**, 449
- Pinzke A., Oh S. P., Pfrommer C., 2013, *MNRAS*, **435**, 1061
- Pinzke A., Oh S. P., Pfrommer C., 2017, *MNRAS*, **465**, 4800
- Planck Collaboration et al., 2016, *A&A*, **594**, A13
- Powell K. G., Roe P. L., Linde T. J., Gombosi T. I., De Zeeuw D. L., 1999, *Journal of Computational Physics*, **154**, 284
- Rieder M., Teyssier R., 2017, *MNRAS*, **471**, 2674
- Röttgering H. J. A., 2010, in ISKAF2010 Science Meeting. p. 50
- Röttgering H., et al., 2011, *Journal of Astrophysics and Astronomy*, **32**, 557
- Sarazin C. L., 1999, *ApJ*, **520**, 529
- Shimwell T. W., et al., 2017, *A&A*, **598**, A104
- Sijacki D., Springel V., Di Matteo T., Hernquist L., 2007, *MNRAS*, **380**, 877
- Sijacki D., Vogelsberger M., Genel S., Springel V., Torrey P., Snyder G. F., Nelson D., Hernquist L., 2015, *MNRAS*, **452**, 575
- Springel V., 2010, *MNRAS*, **401**, 791
- Springel V., et al., 2018, *MNRAS*, **475**, 676
- Vacca V., Govoni F., Murgia M., Giovannini G., Feretti L., Tugnoli M., Verheijen M. A., Taylor G. B., 2011, *A&A*, **535**, A82
- Vazza F., Brüggen M., 2014, *MNRAS*, **437**, 2291
- Vazza F., Gheller C., Brüggen M., 2014a, *MNRAS*, **439**, 2662
- Vazza F., Brüggen M., Gheller C., Wang P., 2014b, *MNRAS*, **445**, 3706
- Vazza F., Ferrari C., Brüggen M., Bonafede A., Gheller C., Wang P., 2015, *A&A*, **580**, A119
- Vazza F., Brüggen M., Wittor D., Gheller C., Eckert D., Stubbe M., 2016, *MNRAS*, **459**, 70
- Vazza F., Brunetti G., Brüggen M., Bonafede A., 2018, *MNRAS*, **474**, 1672
- Venturi T., Giacintucci S., Brunetti G., Cassano R., Bardelli S., Dallacasa D., Setti G., 2007, *A&A*, **463**, 937
- Venturi T., Giacintucci S., Dallacasa D., Cassano R., Brunetti G., Bardelli S., Setti G., 2008, *A&A*, **484**, 327
- Vogelsberger M., Genel S., Sijacki D., Torrey P., Springel V., Hernquist L., 2013, *MNRAS*, **436**, 3031
- Vogelsberger M., et al., 2014a, *MNRAS*, **444**, 1518
- Vogelsberger M., et al., 2014b, *Nature*, **509**, 177
- Weinberger R., et al., 2017, *MNRAS*, **465**, 3291
- Wiener J., Oh S. P., Guo F., 2013, *MNRAS*, **434**, 2209
- Wittor D., Vazza F., Brüggen M., 2016, *Galaxies*, **4**, 71
- Xu H., et al., 2012, *ApJ*, **759**, 40
- Zandanel F., Pfrommer C., Prada F., 2014, *MNRAS*, **438**, 124
- ZuHone J. A., Biffi V., Hallman E. J., Randall S. W., Foster A. R., Schmid C., 2014, in van der Walt S., Bergstra J., eds, *Proceedings of the 13th Python in Science Conference*. pp 103–110
- ZuHone J. A., Brunetti G., Giacintucci S., Markevitch M., 2015, *ApJ*, **801**, 146

## APPENDIX A: SYNCHROTRON RADIATION

### A1 Synchrotron emissivity

To compute the total emitted synchrotron power we assume a relativistic population of electrons in each gas cell whose number density per energy interval is distributed as a power law of the form

$$\frac{dn(\gamma)}{d\gamma} = n_0 \gamma^{-p} \quad \text{for } \gamma > \gamma_{\min}, \quad (\text{A1})$$

where  $\gamma$  is the Lorentz factor,  $n_0$  a normalizing factor (to be determined),  $p$  is the electron spectral index and  $\gamma_{\min}$  is a lower energy cut-off that takes into account the fact that only very energetic electrons ( $\gamma \sim 10^3$ ) contribute significantly to synchrotron emission. We make further assumption that each electron emits at the synchrotron critical frequency  $\nu_s \equiv \gamma^2 \nu_L$ .  $\nu_L$  is the so-called Larmor frequency given by

$$\nu_L = \frac{eB}{2\pi m_e c}, \quad (\text{A2})$$

with  $e$  and  $m_e$  being the electron charge and mass, respectively,  $B$  the intensity of the B field in the cell and  $c$  the speed of light. Under these assumptions we can write the power emitted per unit frequency by a single electron as (see e.g. Longair 2011)

$$P(\nu) = \frac{4}{3} \sigma_T c U_B \beta^2 \gamma^2 \delta(\nu - \nu_s) \approx \frac{4}{3} \sigma_T c U_B \gamma^2 \delta(\nu - \nu_s), \quad (\text{A3})$$

in which  $\sigma_T$  is the Thomson cross section,  $U_B = B^2/(8\pi)$  is the magnetic energy density and the last approximate equality holds in the ultrarelativistic limit  $\gamma \gg 1$ ,  $\beta = v/c \approx 1$ .

The total power radiated per unit frequency and volume by the electron population distributed as in equation (A1) is obtained as

$$\epsilon_{\text{tot}}(\nu) = \int_{\gamma_{\min}}^{\gamma_{\max}} \frac{4}{3} \sigma_T c U_B \gamma^{2-p} n_0 \delta(\nu - \nu_s) d\gamma, \quad (\text{A4})$$

where  $\gamma_{\min}$  and  $\gamma_{\max}$  are the minimum and maximum Lorentz factors of the electron population, respectively. With the change of variable  $\nu' = \gamma^2 \nu_L$  equation (A4) yields

$$\epsilon_{\text{tot}}(\nu) = \frac{2}{3} \frac{\sigma_T c U_B n_0}{\nu_L} \left( \frac{\nu}{\nu_L} \right)^{-\alpha}, \quad (\text{A5})$$

with  $\alpha = (p - 1)/2$ .

We compute the total synchrotron power per unit frequency and volume at  $\nu_0$  over a bandwidth of  $\Delta\nu$  by integrating the power given by equation (A5) over the bandwidth and averaging the resulting total power over  $\Delta\nu$  (see also Xu et al. 2012). This results in

$$\epsilon_{\nu_0} = \frac{2}{3} \frac{\sigma_T c U_B n_0}{\Delta\nu(1 - \alpha)} \left[ \left( \frac{\nu_+}{\nu_L} \right)^{1-\alpha} - \left( \frac{\nu_-}{\nu_L} \right)^{1-\alpha} \right], \quad (\text{A6})$$

where  $\nu_{\pm} = \nu_0 \pm \Delta\nu/2$ . The total synchrotron emission in the target objects is then obtained by multiplying the previous equation by the cell volume and summing over all gas cell contributions. The parameters that we have considered for different radio telescopes are listed in Table A1. We assume that the integration times of the mock observations are the ones necessary to reach the sensitivity reported in Table A1. These can vary between  $\approx 2$  hours per pointing in the case of VLA (Govoni et al. 2001) and up to  $\approx 8$  hours per pointing in the case of LOFAR (Shimwell et al. 2017). The remaining quantities that need to be determined in order to compute the synchrotron emissivity are the spectral index  $\alpha$ , which can be readily fixed from observations (usually  $\alpha > 1$ ), and the electron

Telescope	$\nu_0$ [MHz]	$\Delta\nu$ [MHz]	beam [arcsec]	rms noise [mJy beam <sup>-1</sup> ]
VLA	1400	25	35	0.1
LOFAR-HBA	120	32	25	0.25
ASKAP	1400	300	10	0.01
SKA-LOW	120	32	10	0.02

**Table A1.** Telescope configurations for radio maps. The columns list (from left to right): instrument name, observation frequency, frequency bandwidth, beam size (FWHM), and rms noise. Values for these parameters have been taken from Govoni et al. (2001, VLA; Fig.1 right panel), Röttgering et al. (2011, LOFAR), Norris et al. (2013, ASKAP), and Cassano et al. (2015, SKA; see also Vazza et al. 2015).

density normalization  $n_0$ . In the subsections below we present two different parametrizations to determine the latter quantity.

## A2 Model 1

In our first model we only consider relativistic particles above the low energy cut-off  $\gamma_{\min}$ , which are the only ones that contribute to the emitted synchrotron radiation. To find an expression for  $n_0$  we assume that in each gas cell the energy density in relativistic particles (protons and electrons) is proportional to the magnetic energy density according to

$$(1+k)m_e c^2 n_0 \int_{\gamma_{\min}}^{\gamma_{\max}} \gamma^{-2\alpha} d\gamma = \eta U_B, \quad (\text{A7})$$

where  $k$  is the energy density ratio between (relativistic) protons and electrons and  $\eta$  the ratio between the energy density in relativistic particles and the magnetic energy density. We note that eq. (A7) makes the assumption that protons and electrons are distributed in energy according to the same power law (A1). Equation (A7) yields

$$n_0 = \frac{\eta}{(1+k)} \frac{B^2}{8\pi m_e c^2} \left( \int_{\gamma_{\min}}^{\gamma_{\max}} \gamma^{-2\alpha} d\gamma \right)^{-1} = \frac{\eta}{(1+k)} \frac{B^2}{8\pi m_e c^2} \frac{(2\alpha-1)}{\gamma_{\min}^{1-2\alpha} - \gamma_{\max}^{1-2\alpha}}. \quad (\text{A8})$$

Common choices for the  $\eta$  parameter are those known as minimum energy ( $\eta = 4/3$ , Longair 2011), in which the total energy content in relativistic particles and magnetic fields is minimized at fixed total synchrotron power, and equipartition ( $\eta = 1$ ), in which magnetic fields and relativistic particles have the same energy density. In what follows, we assume that B fields and relativistic particles (protons plus electrons) have the same energy density (i.e.  $\eta = 1$ ), which is justified in galaxy clusters (e.g. Pinzke & Pfrommer 2010; Arlen et al. 2012). Furthermore, we fix  $k = 10$ , consistent with determinations of cosmic rays energy fluxes in the Milky Way and other theoretical work (Enßlin et al. 2011; Vazza & Brüggen 2014; Persic & Rephaeli 2014).

The choice of these parameters implies that, for our cluster sample, about 0.6 per cent of thermal energy in any given cluster is present in the form of relativistic particles. Indeed for our simulated objects the magnetic energy density is only about 1 per cent of the gas thermal energy (see Fig. 6, bottom right-hand panel). Breaking the energetics up in relativistic electron and proton contributions, we find that electrons carry about 0.05 per cent of the cluster thermal energy while protons approximately 0.5 per cent. The proton energy content is in agreement with what has been determined by recent Fermi upper limits. For instance, in the Coma

cluster Brunetti et al. (2017) find that the ratio between the energy density of cosmic rays proton to the gas thermal energy density, albeit dependent on the distance to the centre, is about  $\lesssim 1$  per cent (reaching up to 10 per cent in the outskirts), which is consistent with our modelling. However, in that paper, the spectrum of relativistic particles extends down to  $\gamma = 1$ . This is the major limitation of the present model, since in principle, even though electrons below  $\gamma_{\min}$  do not contribute substantially to the total synchrotron emission, they can nevertheless carry the bulk of the energy of the whole population. We address this limitation of the model in the next section.

Finally, we use as lower and upper limits for the electron Lorentz factor  $\gamma_{\min} = 300$  and  $\gamma_{\max} = \infty$ , respectively. For a justification of the cut-off at low  $\gamma$  see Section A3. The spectral index  $\alpha$  is fixed to 1.7, appropriate for the cluster temperature range ( $T \lesssim 8$  keV) analysed here (see discussion in Feretti et al. 2012, page 15). The parameters thus chosen reproduce fairly well the scaling relation between the total radio power and the X-ray luminosity on galaxy clusters (see Fig. 16 left-hand panel). Indeed, we have used this observational relation, as presented in Feretti et al. (2012), to calibrate the synchrotron emission in our simulations. Figure A1 (top panel, solid lines) shows the main characteristic features of the emitted radiation (described by equation A5) as a function of frequency for three different (constant) magnetic field intensities typical of the ICM for the present model.

## A3 Model 2

In our second model we address the major shortcoming of the model presented in Section A2 by extending the spectrum of relativistic electrons down to  $\gamma = 1$ . To do so we follow Sarazin (1999) and assume that relativistic electrons are injected continuously in the ICM according to

$$Q(\gamma) = Q_0 \gamma^{-2\alpha}, \quad (\text{A9})$$

where  $\alpha$  is the spectral index of the synchrotron radiation,  $\gamma$  is the Lorentz factor, and  $Q_0$  is the electron injection rate per unit volume (which is related to  $n_0$  that needs to be determined). The electron population evolves subject to Coulomb losses (at low energies) and inverse Compton and synchrotron losses (at high energies). If the time-scale of these losses is less than the cluster age (as is usually the case), the electron population reaches a steady state distribution given by (see Sarazin 1999, equation 38)

$$n(\gamma) = \frac{1}{b(\gamma)} \int_{\gamma}^{\infty} Q(\gamma') d\gamma', \quad (\text{A10})$$

where  $b(\gamma)$  is the so-called loss function that parametrizes Coulomb and radiation losses from the ageing electrons. The loss function can be written as (see again Sarazin 1999, equations 6 – 9)

$$b(\gamma) = b_{\text{Coulomb}} + b_{\text{IC+synch}}(\gamma), \quad (\text{A11})$$

with

$$b_{\text{Coulomb}} \simeq 1.2 \times 10^{-15} \left( \frac{n_e}{10^{-3} \text{ cm}^{-3}} \right) s^{-1} = A \left( \frac{n_e}{10^{-3} \text{ cm}^{-3}} \right) s^{-1}, \quad (\text{A12})$$

$$b_{\text{IC+synch}}(\gamma) \simeq 1.37 \times 10^{-20} \gamma^2 \left[ (1+z)^4 + 0.095 \times \left( \frac{B}{1 \mu\text{G}} \right)^2 \right] s^{-1}, \quad (\text{A13})$$



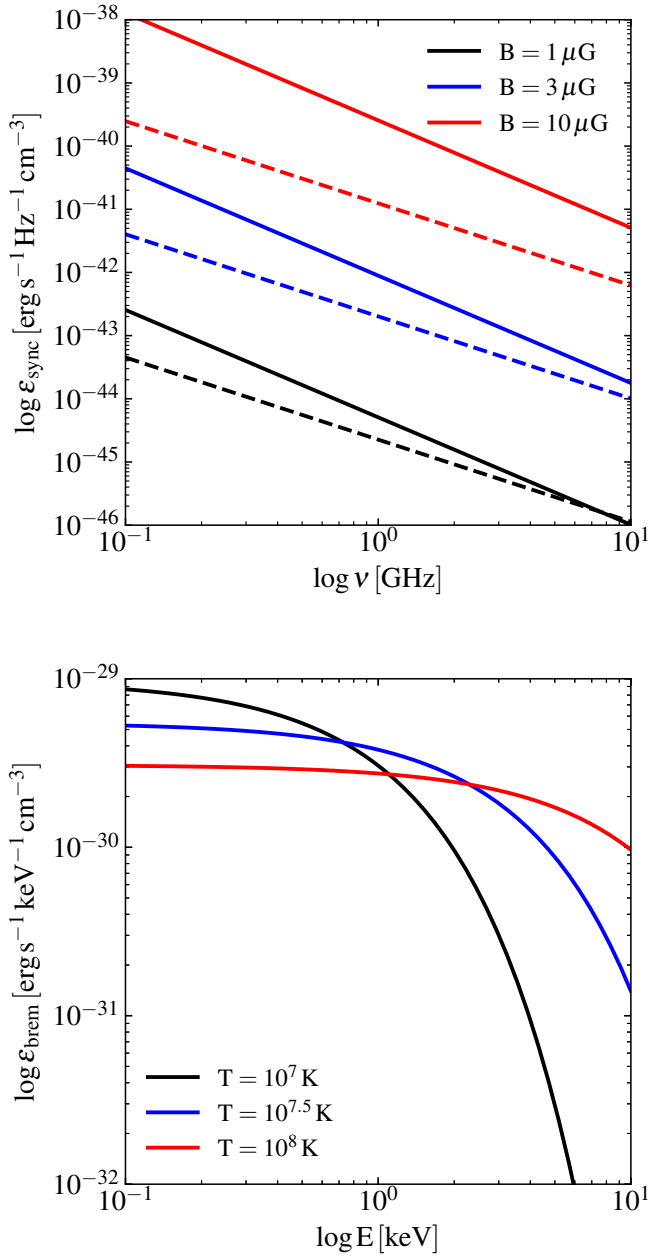


**Figure A1.** Top panel: Volumetric synchrotron emissivity as a function of frequency for synchrotron model 1 (solid lines) and 2 (dashed lines). The emissivity is computed for constant magnetic field intensities as indicated in the legend and with the typical parameters in Section A2 for model 1, whereas the emission for model 2 has been estimated by assuming a value for the gas thermal energy density equal to the magnetic energy contained in the fields listed in the legend and a constant (thermal) electron density  $n_e = 10^{-3} \text{ cm}^{-3}$ . Note the power-law slope of the resulting spectrum (index  $-\alpha$ ) and its strong dependence on the field strength ( $\propto B^{3+\alpha}$ ). Bottom panel: Volumetric bremsstrahlung emissivity as a function of energy for the typical parameters that we have adopted in this work (see Section B). The resulting spectrum is computed for different gas temperature values, as indicated in the legend, and for  $n_H = 10^{-3} \text{ cm}^{-3}$ . Note how the characteristic exponential cut-off at high energies moves towards higher values for increasing gas temperatures.

which represent the expression for the Coulomb and radiation losses due to synchrotron and inverse Compton on the cosmic microwave background photons, respectively. Substituting these expression in eq. (A10), the steady state electron distribution becomes

$$n(\gamma) = \frac{Q_0}{A(2\alpha - 1)} \frac{\gamma^{1-2\alpha}}{1 + (\gamma/\gamma_{\text{br}})^2} = n_0 \frac{\gamma^{1-2\alpha}}{1 + (\gamma/\gamma_{\text{br}})^2}, \quad (\text{A14})$$

with

$$\gamma_{\text{br}} = \left( \gamma^2 \frac{b_{\text{Coulomb}}}{b_{\text{IC+synch}}(\gamma)} \right)^{1/2}. \quad (\text{A15})$$

Please note that  $\gamma_{\text{br}}$  is independent of  $\gamma$ . Please also note that in the asymptotic limit  $\gamma \gg \gamma_{\text{br}}$ , this distribution can be approximated by

$$n(\gamma) \sim n_0 \gamma_{\text{br}}^2 \gamma^{-(1+2\alpha)} \quad (\text{A16})$$

which, modulo the constant factor  $\gamma_{\text{br}}^2$  that can be reabsorbed in the electron normalization, recovers the electron distribution adopted in Section A2. Moreover, for typical cluster conditions at  $z = 0$  ( $n_e = 10^{-3} \text{ cm}^{-3}$ ,  $B = 1 \mu\text{G}$ )  $\gamma_{\text{br}} \simeq 282$ , which justifies our previous value for  $\gamma_{\text{min}}$ .

To fully characterize the model  $n_0$  or alternatively  $Q_0$  must be determined. We do so by imposing that the total energy content in the electrons is a fraction  $\eta$  of the cluster thermal energy per unit volume  $U_{\text{therm}}$  for any gas cell contained in the cluster. This leads to the condition

$$E_{\text{el}} = m_e c^2 n_0 \int_1^\infty \frac{\gamma^{2-2\alpha}}{1 + (\gamma/\gamma_{\text{br}})^2} d\gamma = m_e c^2 n_0 G(\gamma_{\text{br}}, \alpha) = \eta U_{\text{therm}}, \quad (\text{A17})$$

which yields

$$n_0 = \frac{\eta U_{\text{therm}}}{m_e c^2 G(\gamma_{\text{br}}, \alpha)}, \quad Q_0 = A(2\alpha - 1) \frac{\eta U_{\text{therm}}}{m_e c^2 G(\gamma_{\text{br}}, \alpha)}. \quad (\text{A18})$$

From the previous expressions it is also possible to determine the total energy injection rate to sustain the cluster radio emission. The injection rate is given by

$$\dot{E}_{\text{inj}} = m_e c^2 Q_0 \int_1^\infty \gamma^{1-2\alpha} d\gamma = \frac{m_e c^2 Q_0}{(2\alpha - 2)}, \quad (\text{A19})$$

and upon substituting into eq. (A18) one obtains

$$\dot{E}_{\text{inj}} = A \frac{(2\alpha - 1)}{(2\alpha - 2)} \frac{\eta U_{\text{therm}}}{G(\gamma_{\text{br}}, \alpha)}. \quad (\text{A20})$$

The total energy (in terms of the cluster thermal energy) needed to sustain the cluster radio emission can be found by multiplying the previous expression by  $t_{\text{Hubble}} \sim 10 \text{ Gyr}$ . This yields

$$\frac{E_{\text{inj}}}{U_{\text{therm}}} = A t_{\text{Hubble}} \frac{(2\alpha - 1)}{(2\alpha - 2)} \frac{\eta}{G(\gamma_{\text{br}}, \alpha)}, \quad (\text{A21})$$

which for typical galaxy cluster parameters at  $z = 0$  ( $n_e = 10^{-3} \text{ cm}^{-3}$ ,  $B = 1 \mu\text{G}$ ) and  $\alpha = 1.3$  becomes

$$\frac{E_{\text{inj}}}{U_{\text{therm}}} = 0.04 \left( \frac{\eta}{10^{-3}} \right). \quad (\text{A22})$$

This is only a small fraction of the total cluster energy and thus the model is energetically feasible. For the results presented in the paper we have adopted  $z = 0.2$ ,  $\alpha = 1.3$ ,  $\eta = 6 \times 10^{-3}$ , whereas the (thermal) electron density  $n_e$  and  $B$  field entering the loss equations are the volume-weighted average within the virial radius of each cluster. In this way the total energy requirements of the model for a Hubble time are about  $\sim 6\%$  of the cluster thermal energy, and

relativistic electrons with Lorentz factors in the range  $\gamma \in [1, \infty]$  contain presently as much energy as the magnetic field in each cluster. The main features of the emitted radiation as a function of frequency are shown in Figure A1 (top panel, dashed lines) by assuming a value for the gas thermal energy density equal to the magnetic energy contained in the field strengths listed in the legend and a constant (thermal) electron density  $n_e = 10^{-3} \text{ cm}^{-3}$ . Finally, we would like to note that, with the choice of the fiducial parameters, relativistic particles carry approximately the same fraction of the total cluster energy in models 1 and 2. However, the major difference is that, while in model 1 this is the total energy of ultrarelativistic ( $\gamma > 300$ ) protons and electrons, in model 2 only relativistic electrons, with a spectrum extending down to  $\gamma = 1$ , are present. The total energy carried by ultrarelativistic electrons (the only ones that contribute in a significant way to synchrotron emission) is about the same in both models, which implies similar levels of radio emissivity.

## APPENDIX B: BREMSSTRAHLUNG RADIATION

To compute the X-ray emission from the galaxy cluster sample selected in this work, we make the assumption that the X-ray radiation is produced by bremsstrahlung from thermal electrons in the hot gas. We note that this model is somewhat a simplification because, for instance, it does not attempt to model line emission, which can be important in lower mass (colder) systems. However, it is accurate enough to investigate the scaling relations that we have presented in the paper.

We compute the volumetric bremsstrahlung emissivity as (see e.g. Kannan et al. 2016b)

$$\epsilon_\nu = 6.8 \times 10^{-38} T^{-1/2} \exp\left(-\frac{h\nu}{kT}\right) Z^2 g_{\text{ff}} n_e n_i, \quad (\text{B1})$$

where  $T$  is the gas temperature,  $h$  is the Planck constant,  $\nu$  the frequency of the radiation,  $k$  the Boltzmann constant,  $Z$  the mean ionic charge,  $g_{\text{ff}}$  the mean gaunt factor, and  $n_e$  and  $n_i$  the number density of electrons and ions, respectively. Figure A1 (bottom panel), show the characteristic resulting spectrum for three different values of the gas temperature, as indicated in the legend, in terms of  $E = h\nu$ . A constant hydrogen number density of  $10^{-3} \text{ cm}^{-3}$  is assumed (see below for the values of the remaining parameters).

To determine the X-ray luminosity of any given gas cell  $j$  we integrate equation (B1) over a prescribed energy range  $[E_{\text{low}}, E_{\text{high}}]$  and multiply by the cell volume, obtaining

$$L_{j,[E_{\text{low}}, E_{\text{high}}]} = 6.8 \times 10^{-38} \frac{kT_j^{1/2}}{h} \left[ \exp\left(-\frac{E_{\text{low}}}{kT_j}\right) - \exp\left(-\frac{E_{\text{high}}}{kT_j}\right) \right] Z^2 g_{\text{ff}} \frac{X_e}{(X_i + X_e)^2} \left( \frac{\rho_j}{\mu_j m_p} \right)^2 V_j. \quad (\text{B2})$$

In equation (B2), the subscript  $j$  indicates quantities associated to a single gas cells,  $V_j$  is the cell volume,  $\rho_j$  the gas density,  $\mu_j$  the gas mean molecular weight, and  $X_i$  and  $X_e$  are the ratios  $n_i/n_H$  and  $n_e/n_H$ , with  $n_H$  being the hydrogen particle density. We fixed the free parameters in equation (B2) to  $Z = \sqrt{1.15}$ ,  $g_{\text{ff}} = 1.3$ ,  $X_i = 1.079$ ,  $X_e = 1.16$ , which are appropriate for a fully ionized gas with primordial composition. We checked, with the `PYXSIM` package (ZuHone et al. 2014), that metal lines do not contribute significantly

to the total X-ray emission in the virial mass range selected for our analysis.

## APPENDIX C: GENERATION OF SURFACE BRIGHTNESS MAPS

We now briefly describe the procedure that we have used to create radio and X-ray emission maps presented in this work. In practice, we have adopted the following steps:

(i) given the radio or the X-ray emissivity of gas cells, we have projected this quantity on a uniform grid, obtaining the radio or X-ray luminosity per unit area;

(ii) by assuming a fiducial redshift (we have adopted a value of 0.2, which is the average redshift of detected radio haloes, Feretti et al. 2012), we have computed the luminosity and angular diameter distance for the cosmology adopted for IllustrisTNG; in this way surface brightness in the appropriate observational units can be determined;

(iii) radio maps are smoothed via a convolution with a Gaussian kernel to the nominal resolution of the radio telescope given by its FWHM beam size; we recall that the relation between the dispersion of the Gaussian and the beam size is given by

$$\sigma_b = \frac{b_{\text{FWHM}}}{2(\ln 2)^{1/2}}. \quad (\text{C1})$$

Sensitivity limits of the different instruments are presented as rms noise in Table A1 for radio emission (see Vazza et al. 2015, and references therein). For X-rays, we have adopted the typical *Chandra* ACIS background  $1.3 \times 10^{-12} \text{ erg s}^{-1} \text{ arcmin}^{-2}$  (Anderson & Bregman 2010). We convert it to a background surface brightness by dividing by the effective telescope area, which we assume to be  $200 \text{ cm}^2$  (see again Anderson & Bregman 2010). The X-ray emission is detected if the surface brightness of a given pixel is above 0.3 times the background value thus determined. Please note that these brightness cuts are only used to produce the maps and are not imposed to compute the total X-ray luminosities.

This paper has been typeset from a  $\text{\LaTeX}$  file prepared by the author.